Effects of Radiation and EGR on Pollutant Formation in High-Pressure Constant Volume Spray Combustion

Khaled Mosharraf Mosharraf Mukut
Marquette University

EFFECT OF RADIATION AND EGR ON POLLUTANT FORMATION IN HIGH-PRESSURE CONSTANT VOLUME SPRAY COMBUSTION

by

Khaled Mosharraf Mukut

A Thesis submitted to the Faculty of the Graduate School,
Marquette University,
in Partial Fulfillment of the Requirements for
the Degree of Master of Science

Milwaukee, Wisconsin

August 2019

ABSTRACT
EFFECT OF RADIATION AND EGR ON POLLUTANT FORMATION IN HIGH-PRESSURE CONSTANT VOLUME SPRAY COMBUSTION

Khaled Mosharraf Mukut

Marquette University, 2019

Soot formation is a complex process and the actual soot formation methodology is still a mystery. Numerically modeling of soot requires successful coupling of turbulence, chemistry and radiation modeling. In the present study, a comprehensive sensitivity study is conducted to see the effect of radiation and exhaust gas recirculation (EGR) on soot and NO_X formation in a high pressure spray combustion scenario.

The spray-A case (n-dodecane as fuel) from Engine Combustion Network (ECN) is used as the target condition. Two different soot modeling approaches have been considered: a semi-empirical two-equation model and a method of moments with interpolative closure (MOMIC). A multiphase photon Monte Carlo (PMC) solver with line-by-line (LBL) spectral database is used to resolve radiative heat transfer. Results show that, effect of radiation on soot is minimal in spray-A configuration. Inclusion of radiation modeling, on the other hand, marginally reduce NO prediction. Both peak soot and NO formation increases with O_2 content in EGR. Oxygen content of EGR is found to have significant effect on soot sizes as the mean soot diameter increases along with considerable widening of the diameter distribution with the increase of O_2 percentage.

ACKNOWLEDGMENTS

Khaled Mosharraf Mukut

At first, I would like to express my sincere gratitude to my thesis supervisor Dr. Somesh P. Roy for his continuous support of my MS study and research. His patience, motivation and guidance helped me a lot in my journey. He continuously enabled me to make this my own work and guided me in the right direction whenever I needed it.

I would also like to thank Dr. Simcha Singer and Dr. John Borg for their valuable comments on this thesis.

DEDICATION

I would like to dedicate this work to my ever-supporting family and friends.

Thank You

TABLE OF CONTENTS

LIST OF TABLES

LIST OF FIGURES

CHAPTER 1

INTRODUCTION

1.1 Background

Internal combustion engines play an important role in transportation and power generation sectors. Combustion processes are often accompanied by large amount of harmful emissions like soot and NO_X. Therefore, it is very important to understand the outcomes of combustion processes and to be able to predict the effect of different operating conditions typically found in internal combustion engines. Reducing the amount of pollutant formation while keeping the engine efficiency unaffected has been a topic of great interest among the engine researchers in recent decades.

1.2 Motivation

Radiative heat transfer can be a important mode of heat transfer in large diesel engines because of high temperature and pressure. In the previous literature , it is reported that, radiation may account for more than 40% of the overall heat loss [10, 11] in IC engines. Because of this, the temperature distribution can be affected significantly and thus the pollutant formation like soot and NO_X can be significantly affected. Musculus [12] reported that, a change in 20-25 K in peak temperature due to radiative heat transfer can impact NO_X production by as much as 25%. Exhaust gas re-circulation on the other hand, have been used for a long time to reduce soot and NO_X formation in diesel engines.

A number of previous studies have been conducted previously regarding the soot and NO_X formation in diesel engines focusing on radiative heat transfer [13, 14, 15, 12, 16]. Almost all of these studies make assumptions like optically

thin medium which is not appropriate for a high pressure combustion scenario [17]. To the best of our knowledge, no study has been conducted so far by coupling a fully detailed radiation solver with chemistry in high pressure scenario. In the present study, a state of the art photon Monte Carlo line-by-line (PMC/LBL) multiphase radiation solver is used to investigate the effect of radiation in engine combustion network's (ECN) spray-A high pressure constant volume combustion chamber in terms of soot and NO_X formation.

1.3 Literature Review

Exhaust gas recirculaiton (EGR) is often used to reduce the NO_X emission in modern internal combustion engines. Use of EGR dilutes the O_2 concentration which results in a lower flame temperature in the combustion chamber [18, 19]. Addition of EGR tends to increases soot formation which results in an increase in radiative heat loss from soot [20].

The presence of high pressure and temperature along with spray and particulate matters makes the combustion dynamics very complex in internal combustion engines. The complex multiphysics interaction makes it further difficult to understand and model the fundamental processes in engine-relevant conditions. Although the radiative heat transfer can contribute 12%-15.5% of the total thermal heat loss [13, 21] in diesel engines, radiation modeling is often neglected or simplified in engine simulations.

The present work focuses on numerical modeling of high-pressure, constant volume spray combustion experiments reported by engine combustion network (ECN) [22]. Liquid n-dodecane spray (ECN spray-A) is used as the fuel and different exhaust gas recirculation (EGR) configurations are considered. A series of previous studies have been conducted on ECN spray-A case. Som et al. [23] studied several ECN combustion chamber and proposed baseline parameters

for the numerical approach to model those cases. Fernandez et al. [24] used a transported probability density function (TPDF) solver to investigate the soot formation in ECN spray-A case. To resolve the turbulence radiation interaction (TRI) properly they used a photon Monte Carlo/line-by-line (PMC/LBL) radiation solver. However, the radiation solver was not coupled with the gas phase chemistry for all simulations in that study and the effect of EGR was not investigated. Haworth and coworkers [25, 26] reported that nongray radiation contributes not only to the wall heat loss but also in the spatial redistribution of temperature. Chishty et al. [27] also studied the importance of radiative heat transfer using three different radiation model for spray-A and concluded that the effect of turbulence radiation interaction (TRI) is important and it increases the overall radiation emission. Recently, they also investigated the soot formation in spray-A case with turbulent chemistry interaction (TCI) [28]. They used a two-equation semi-empirical soot model and assumed an optically thin radiative heat transfer configuration. However, due the presence of high pressure inside the combustion chamber, the optically thin approximation does not hold true [24]. In another recent study, Yue and Reitz [29] used a discrete ordinate method (DOM) to study the effect of radiative heat transfer on soot and NO_X formation and reported that, radiation can influence the engine-out soot production by as much as 50% under certain conditions.

Although different numerical studies have been conducted regarding TCI, gas phase radiation and spray radiation individually, to the best of our knowledge, no study has been conducted yet coupling the multiphase radiation with soot models in spray-A spray combustion cases. As some researchers have pointed out, including spray droplets in radiation transfer may have some effect on pollutant formation under certain conditions [30, 31]. In this work, we systematically investigate the effect of multiphase radiation, soot model

sensitivity and different EGR oxygen concentration on pollutant production in spray-A case.

In this work, a Reynolds average simulation framework is used along with a photon Monte Carlo line by line (PMC/LBL) detailed multiphase radiation solver. Both spray and gas phase radiation is studied in depth for different EGR configurations and their effect on soot and NO_X formation. The soot formation and distribution is studied in details using a detailed method of moment soot model. The novelty of the present study lies in systematic study of the local and global effects of both spray and gas phase radiation under different EGR configurations, and detailed investigation of soot characteristics and size statistics at different stages of combustion.

1.4 Organization

In this study, a comprehensive sensitivity study of pollutant formation behavior is conducted. In order to systematically present the content of this study, the thesis is divided into several chapters. The overall study is divided in two segments: (1) Pollutant (soot and NO_x) formation and (2) Evolution of soot particle statistics. Chapter 2 of this thesis discusses different numerical modeling approach for relevant components. Chapter 3 discusses the soot and NO_X formation sensitivity with radiation, soot models and EGR respectively. Chapter 4 investigates the evolution of soot particle size distribution in details at different EGR configurations. Finally, chapter 5 and 6 summarise the study and present some future recommendations. The chapter 3 and 4 are mostly taken from the author's under-review article [32].

CHAPTER 2

NUMERICAL MODELS

2.1 Spray Models

Spray formation is a complex process. Many important details about the physics of spray formation is still unknown. Spray formation process starts due to a high pressure difference across an orifice. Due to the large drop in pressure the liquid gains high velocity and this leads to local drop in the pressure below the vapor saturation pressure of the liquid. Therefore, the liquid evaporates and form spray. This phenomenon is known as cavitation which is closely related to superheated atomization [33].

The spray formation process can be analysed based on the following stages: development of jet, formation of liquid sheets from the jet, disintegration into large droplets (primary break-up), formation of smaller droplets from the larger ones (secondary break-up) [34, 35]. Almost all the quantitative spray models assumes direct disintegration of the liquid jet into droplets due to the development of jet instabilities [36]. A comprehensive review of the spray models can be found [37].

The atomization behaviour of liquid spray can be described in terms of multiphase flow where the liquid parts remain in the form of droplets and the gas phase is represented as a continuum. The disintegration of the spray occurs when the disruptive forces exceed the surface tension of the liquid. The disruptive forces such as aerodynamic force, centrifugal force, surface shear force etc. can create oscillation in the interface which results in the break up of the liquid into smaller droplets. This initial break up phenomenon is referred as the primary break up of the spray. If the droplet size is larger than a critical droplet size, they

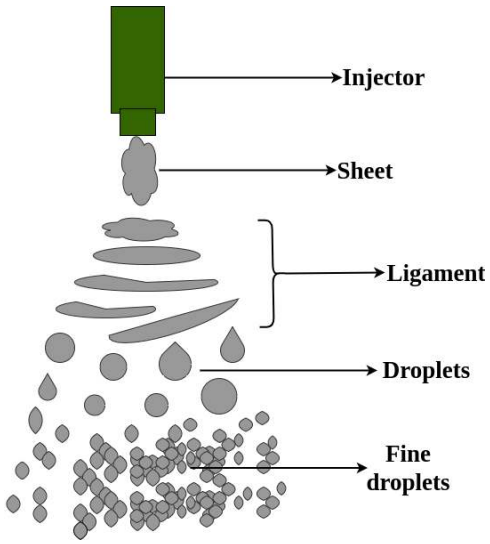

Figure 2.1: Schematic of spray atomization

may disintegrate further to create smaller droplets. This is referred as secondary break up of spray. Figure 2.1 depicts the schematic of spray atomization process. The droplet size distribution in the spray is determined by the flow characteristics of both disintegrating regime. The analysis of the spray is done using several non-dimensionless quantity as listed below:

$$\text{Liquid Reynolds Number} : Re_l = \frac{\rho_l u_l d_l}{\mu_l} \tag{2.1}$$

$$\text{Liquid Weber Number} : We_l = \frac{\rho_l u_l^2 d_l}{\sigma} \tag{2.2}$$

$$\text{Aerodynamic (gas) Weber Number} : We_g = \frac{\rho_g u_{rel}^2 d_l}{\sigma} \tag{2.3}$$

$$\text{Ohnesorge number} : Oh = \sqrt{\frac{We_l}{Re_l}} \tag{2.4}$$

$$\text{Discharge Coefficient} : C_d = \frac{vl}{\sqrt{\frac{2\Delta P}{\rho_l}}} \tag{2.5}$$

$$\text{Cavitation Parameter} : K = \frac{2(P_l - P_g)}{\rho_l v^2} \tag{2.6}$$

Where,

ρ_l and ρ_g = density of liquid and gas respectively,

ΔP = (P_l - P_g) = injection pressure,

u_l = liquid velocity,

u_{rel} = relative velocity ,

μ_l = dynamic viscosity,

σ = surface tension co-efficient,

ν = kinematic viscosity,

d_l = diameter of nozzle

Spray modeling approaches can be divided into two methodologies: Eulerian and Lagrangian [38]. In Eulerian approach, the spray is treated as a continuum or a second phase of a multiphase flow. On the other hand, the Lagrangian approach, the spray droplets or parcels (collection of equal-size droplets) are individually tracked alongside the continuum. The Lagrangian methods emphasize on modeling the jet and droplet breakup. The spray droplets start disintegrating near the nozzle exit in the primary breakup region. Further downstream, the larger droplets transition into smaller droplets which is known as the secondary break up of spray. The jet is modelled by approximating a chain of droplets where the initial diameter is assumed to be equal or slightly less (if the cavitation effects are taken into account) than the nozzle diameter.

Usually, blob injection model is used to describe injection where the computational parcels are subjected to surface instabilities due to environmental interactions. The classical wave model for spray is therefore based on the temporal stability analysis of the Kelvin-Helmholtz instability for a round jet of

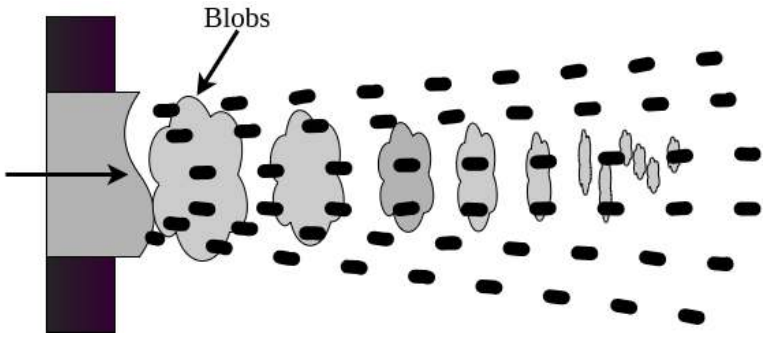

Figure 2.2: Schematic of Blob injection model

liquid with an inviscid outer gas phase [1]. The liquid core maintains constant velocity except for the liquid-gas interface where the velocity is assumed zero.

2.1.1 Primary Break-up Model

The main objective of the primary break-up model is to determine the starting condition for the droplets leaving the nozzle such as the initial parcel diameter, velocity and spray angle. These parameters are determined by both the nozzle internal flow and liquid-vapor interaction. There are several models available for the primary break up model, e.g. Blob method, LISA (Linearized Instability Sheet Atomization) model, turbulence induced atomization etc. A comprehensive review of these models can be found in Baumgarten et al. [39]. Among the primary break-up models, blob atomization model [5, 40] is the mostly used one.

Blob injection model describes the spray jet in terms of continuously injecting large drops (blobs) into the gas-phase. The diameter of the blobs are in the same order as the nozzle exit diameter. The frequency of the blob introduction is controlled by the spray injection rate. Ideally, the blobs are spherical in shape and maintain constant density (ρ). The spray angle is either specified of calculated from empirical relations. The flow inside the nozzle is assumed non-cavitating and hence the velocity of the blob injection can be approximated

using conservation of mass:

$$U_{P,initial}(t) = \frac{\dot{m}_{nozzle}(t)}{A_{nozzle}\rho} \tag{2.7}$$

Where, $\dot{m}_{nozzle}$ is the mass flow rate through nozzle and A_{nozzle} is the cross-sectional area of the nozzle.

Based on the different values of Reynolds number and Ohnesorge number the primary atomization falls into three different regimes:

- **Rayleigh regime** (low-Reynolds number): the droplet break-up occurs due to surface tension effect and thus create fairly identically sized spherical primary droplet
- **Aerodynamic regime** (medium-Reynolds number): the droplet break-up is influenced by aerodynamic forces.
- **Atomization regime** (high-Reynolds number): the droplet break-up is spontaneous as soon as it leaves the nozzle exit.

The transition regime between Rayleigh-Aerodynamic and Aerodynamic-Atomizatoin regime marked by the transition liquid Weber number (We_t) defined by equations 2.8 and 2.9 respectively:

$$We_t = \frac{1.74 \times 10^4}{Re_l^{0.5}} \tag{2.8}$$

$$We_t = \frac{9.4 \times 10^5}{Re_l^{0.5}} \tag{2.9}$$

2.1.2 Secondary Break-up Model

As discussed earlier, the secondary break-up of droplets is defined as the disintegration of the primary droplets. This secondary disintegration occurs due to turbulence, mass/heat transfer, relative velocity etc. The secondary break-up is

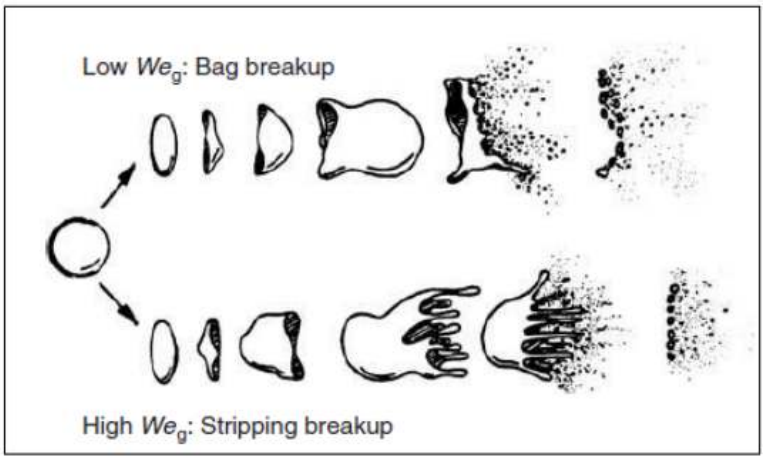

Figure 2.3: Secondary break up modes [5]

characterised by gas Weber number (We_g). The break-up happens when the gas Weber number exceeds a critical value. Viscosity can also affect the secondary break-up characteristics if the Ohnesorge number (Oh) exceeds 0.1 and the effect increases with Weber number (We_g) and the break-up mechanism varies at different regimes, e.g.

- Vibrational break-up ($We_g < 12$)
- Bag break-up ($12 < We_g < 50$)
- Bag and stamen break-up ($50 < We_g < 100$)
- Sheet stripping ($100 < We_g < 350$)
- catastrophic break-up ($350 < We_g$)

The regimes for $We < 100$ are commonly known as bag break-up and $We > 100$ are known as stripping (shear) break-up as shown in figure 2.3. Bag break-up occurs due to Kelvin-Helmholtz (KH) instability which is caused by parallel shear flow. On the other hand, the stripping break-up occurs due to Rayleigh Taylor (RT) instability caused due to cross flow. The timescale (t^*) for secondary break-up is defined as equation 2.10:

$$t^* = \frac{d_0}{u_{ref}} \sqrt{\frac{\rho_l}{\rho_g}} \tag{2.10}$$

Where,

d_0 = wavelength of the fastest growing wave,

u_{ref} = jet velocity.

The computational models for the secondary break-up includes the following parameters:

- calculate the Weber number to check whether break-up occurs or not
- estimation of break-up time
- droplet size distribution
- spatial distribution and velocity of the droplet after break-up

The contemporary literature provides a number of models to describe the secondary break-up process, i.e. Reitz-Diwakar model [40], Taylor analogy break-up (TAB) model [41], cascade atomization and break-up (CAB) model, Schmehl break-up model [42], KH-RT model etc.

As an example, Reitz-Diwakar break-up model [40] will be briefly discussed here. This model differentiates between two break-up regimes, bag break-up and strip break-up, based on a critical Weber number, We_{cric}. It solves a differential equation (equation 2.11) to resolve particle radius:

$$\frac{dr_p}{dt} = -\frac{(r_p - r_{stable})}{t^*} \tag{2.11}$$

where, r_p and r_{stable} are the droplet radii before and after secondary break-up and t^* is the characteristic break-up time. The characteristic time for break-up varies for different break-up regimes.

For bag break-up ($We < We_{cric}$),

$$\begin{aligned} t^* &= C_1\sqrt{\frac{\rho_p r_p^3}{2\sigma}} \\ r_{stable} &= \frac{6\sigma}{\rho_g V_{slip}^2} \end{aligned} \tag{2.12}$$

For stripping break-up ($\frac{We}{\sqrt{Re}} > C_{s1}$)

$$t^* = C_2 \frac{r}{V_{slip}} \sqrt{\frac{\rho_p}{\rho_g}}$$
$$r_{stable} = \frac{\sigma^2}{2\rho_g^2 V_{slip}^3 v} \tag{2.13}$$

The standard model constant for Reitz-Diwakar model [40] are shown in Table 2.1:

Table 2.1: Standard model constant for Reitz-Diwakar secondary break-up model [1]

Constant	**Name**	**Value**
C_1	Time factor for bag break-up	π
C_2	Time factor for stripping	20
We_{cric}	Critical Weber number for bag	6.0
C_{s1}	Weber number factor for stripping	0.5

2.2 Radiation Models

Radiation is the fastest mode of heat transfer and it plays a major role in high temperature combustion scenarios. Radiation becomes more important in situation when the pressure and temperature are high. It also interacts with the turbulence field because of the dispersion of relevant species under the influence of a turbulence field. This interaction of radiation and chemistry is referred as the turbulence radiation interaction (TRI) in the contemporary literature .

The radiation heat transfer is governed by the radiative transfer equation (RTE) as shown in equation 2.14. It is a six-dimensional integro-differential equation. Due to the high dimensionality of the equation, it is almost impossible to evaluate the exact solution of the RTE. Therefore, in most of the combustion

scenarios, radiation is often neglected [43, 44, 45] or crudely simplified [46, 47]. This leads to over-or under-estimations of the temperature fields.

$$\frac{1}{c}\frac{\partial I_\eta}{\partial t} + \frac{\partial I_\eta}{\partial s} = J_\eta - k_\eta I_\eta - \sigma_{s\eta} I_\eta + \frac{\sigma_{s\eta}}{4\pi}\int_{4\pi} I_\eta(\hat{S}_i)\phi_\eta(\hat{S}_i, \hat{S})d\Omega_i \tag{2.14}$$

Where,

ϕ_η = scattering phase function,

η = wavenumber,

c = velocity of light,

k_η = absorption coefficient,

$\sigma_{s\eta}$ = scattering coefficient,

J_η = emission coefficient and

I_η = radiation intensity.

Different assumptions can be made to simplify the RTE. Based on the assumptions made and strategy for solving, there exists several radiation solvers:

- **Discrete transfer radiation model (DTRM) [48]:** This model assumes that, all the radiation leaving a surface within a range of solid angle can be approximated by a single ray. The accuracy of the model increases with the number of ray traced and computational mesh. This model assumes diffused surfaces and non-scattering gray medium.
- **Discrete ordinate method (DOM) [49]:** This model transforms the RTE into a set of partial differential equations, which makes it easy to solve and computationally economic. The partial differential equations separates the spatial and directional dependencies of the RTE. Thus, the entire radiative intensity is discretized into a finite number (N) of solid angles. Number of ordinates, N represents the number of discritization of the whole solid angle

(4π) space and this yields N partial differential equations. The accuracy of the model increases with N and so does the computational cost.

- **Spherical harmonics [50, 51, 52]:** The radiative intensity can be represented in terms of a set of PDEs and separates the spatial and directional dependency through a convergent infinite series of orthogonal spherical harmonics (function of direction only) and intensity coefficients (function of space only). Basically, the deviation of local intensity is represented in terms of local gradient. This model assumes isotropic radiative heat transfer. This model is also referred to as P_N model where N refers to the order. Usually, odd orders of spherical harmonics is more accurate than the next higher even order [53]. In practice, P_1 model is the most implemented.
- **Statistical Models:** Due to high dimensionality of the RTE, statistical Monte Carlo approach is the most ideal for accurately resolve the RTE. These models are implemented in a stochastic manner by means of tracing individual photons and accounting for their energy content and evolution. The present study implements one such model: the state of the art statistical Monte Carlo Ray Tracing (MCRT) model [30] for resolving radiative heat transfer. In this model, a bunch of photon bundles are randomly generated based on the temperature inside simulation domain. The individual photon rays are traced and their energy is accounted for considering absorption, emission, transmission, scattering etc. This is done several times in each timestep and the statistical average gives the actual radiative heat transfer. The accuracy of the model depends on the total number of photon rays generated and the number of statistical runs. With high enough number of rays and statistical runs, this model can resolve the RTE exactly. However, the computational cost increases with the total number of rays. A line by

line (LBL) spectral database [54] is used in this study to account for the absorption co-efficient of the participating medium.

2.3 Soot Models

Soot is primarily carbon particles formed during incomplete combustion of hydrocarbons and this remains one of the least solved problems of combustion. Soot formation is a very complicated process and the exact science behind this is still incomplete. Soot formation is a gradual process and occurs in several stages. Although the exact stages of soot formation are not yet resolved, it is well established that acetylene acts as a precursor to soot formation. The soot formation starts with the formation of acetylene molecules which eventually forms benzene and benzenoid molecules. This leads to the formation of Polycyclic Aromatic Hydrocarbons (PAHs). These PAH molecules collides with each other and forms the first soot particles. This process is called nucleaiton. These PAH molecules further collide with the newly formed soot particles and thus the soot particles grow and evolve. The growth of the soot particle is fractal like. The size distribution of soot particle gives us valuable insight into the physics of their formation. Unfortunately, simpler soot models (empirical and semi-empirical models) can't give us this information. They only provide the number density and mass fraction characteristics without giving any information about their size, shape, distribution surface characteristics. That's where detailed soot model comes into play. The typical soot particles are composed of roughly eight parts of carbon and one part of hydrogen (soot density 1.84701 g/cm^3 [55]). The initial soot particles nucleate within the fuel-rich regions where the temperature is high. The hydrogen content in newly formed spherical soot particles are the highest. Eventually, the carbon fraction increases as it grows into necklace type agglomerates. The evolution of soot particles from gas phase to

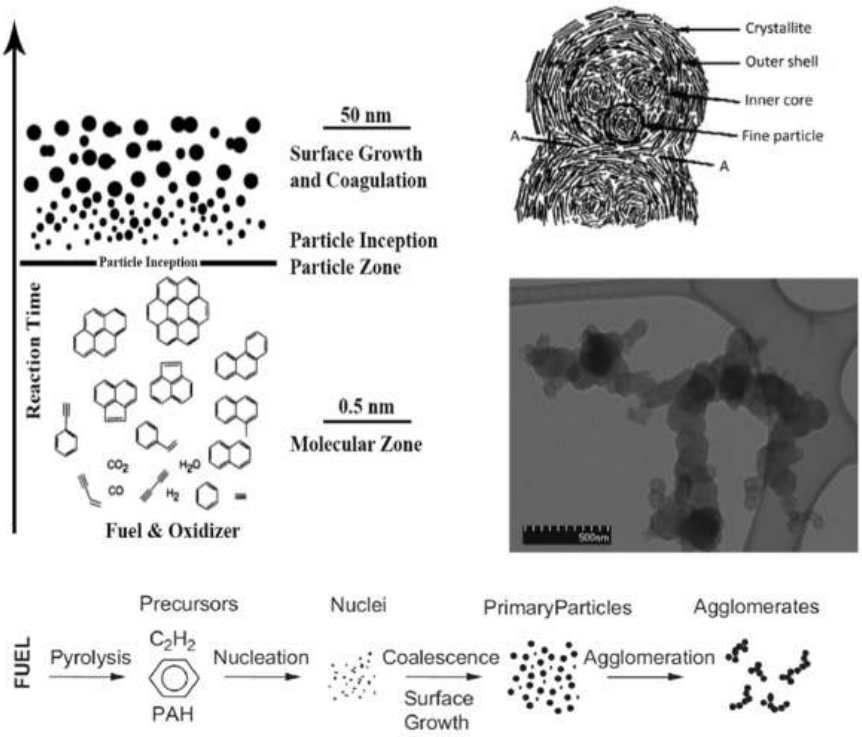

Figure 2.4: Schematic of soot formation pathway [6, 7]

solid agglomerates can be summarized as the following five steps [7, 56] and shown in figure 2.4:

1. Inception of the soot precursors (e.g. acetylene and PAHs) by means of pyrolysis.
2. Nucleation of soot precursor molecules to form the first soot particles.
3. Soot surface growth by adsorption of gas phase PAHs into the soot particles.
4. Coagulation of smaller soot particles due to Brownian motion and formation of soot agglomerates.
5. Oxidation of soot particles with time.

Chemistry affects the growth of soot particle evolution due to different surface reactions. The gas phase acetylene is the major species that reacts with the soot surface. The PAHs may also play a key role in soot formation. These precursors react with the active sites on the particle surface. This results in the

surface and volume growth. Alongside this, the soot particles are also oxidized by oxygen and hydroxyl radicals at the same time. The soot particle cannot grow indefinitely due to surface oxidation. These surface reactions are directly proportional to the soot surface area and morphology.

The uncertainty in measurement methodology and lack of an established theoretical background makes soot modeling a daunting task. Soot formation during combustion depends on several factors, for example: stoichiometry, laminar or turbulent nature of the flow, pressure, radiation etc. The process is stochastic in nature due to the randomness involved in Brownian collision, coagulation and surface growth uncertainty. Several approaches have been attempted over the years which include different level of complexity. As discussed in the earlier section, based on the method used, the soot models can be broadly classified into three major groups, namely empirical, semi-empirical and detailed soot models [57]. The later section of this review will attempt to discuss the specifics of these soot models and their evolution.

2.3.1 Empirical Soot Models

Empirical soot models are developed based on different experimental correlations. For different configurations, soot is initiated by different events. For example, in premixed flame the soot production begins at a threshold equivalence ratio and in diffusion flame soot is measured in terms of the flame height at which soot is emitted, i.e. sooting height. Calcote and Manos [58] used a threshold sooting index (TSI) for soot prediction for both premixed and diffusion flames. TSI can predict a flame's sooting tendency by considering both the threshold equivalence ratio, (ϕ). Two calibrated model constants (a and b) are used to relate both premixed and diffusion flames. Equation 2.15 shows the correlation [59, 60] between TSI and ϕ for a mixture of fuels.

$$TSI = ab\phi_c$$

$$TSI_{mix} = \sum X_i TSI_i \tag{2.15}$$

The soot formation in engine type environment is more complex because of the dependency on temperature, pressure and equivalence ratio etc. The soot formation in engine type of simulation depends of engine loads and different speeds. The rate of soot formation in these cases are assumed to be controlled by the soot inception rate. Khan et al. [61] proposed an Arrhenius type equation for a soot model in engine simulation as shown in equation 2.16.

$$\frac{dM_s}{dt} = c\frac{V_u}{V_N TP} P_u \chi^n exp(\frac{-E}{RT_u}) \tag{2.16}$$

Where,

M_s = soot mass loading [kg/m^3] ,

C,n = model constant [experimentally calibrated],

V_u = volume of soot formation zone [m^3] ,

V_{NTP} = volume of cylinder content at NTP [m^3],

P_U = partial pressure of unburnt fuel (p_a),

χ= equivalence ratio of unburnt fuel,

E = activation energy ,

T_u = local temperature [K].

2.3.2 Semi-empirical Soot Models

The empirical soot models are very rudimentary and cannot predict any physical and chemical aspects of soot production. On the other hand, to investigate the actual dynamics of soot formation several complicated modeling parameters have to be added. Semi-empirical soot models are developed to meet

this dilemma in midway. While, these semi-empirical approximations can predict some physical and chemical dynamics of soot production, they still depend on experimental correlations.There are different formulations of semi-empirical soot models. All of them adopts a set of PDEs to capture the soot dynamics. Usually, two different PDEs are modelled: one for soot number density and the other for the soot volume or mass fraction [57, 62, 63, 64]. As an example, a widely used two-equation semi-empirical model developed by Leung et al. [63] is discussed briefly. The model used a pair of partial differential equations which describes the number density of soot particle (n) and soot mass fraction (Y_s) as shown in equation 2.17.

$$\begin{aligned} \frac{\partial \rho Y_s}{\partial t} + \frac{\partial \rho Y_s u_i}{\partial x_i} &= -\frac{\partial}{\partial x_i}(\rho Y_s V_{t,i}) + \dot{\omega_s}'' \\ \frac{\partial}{\partial t}(\rho \frac{n}{N_A}) + \frac{\partial}{\partial x_i}(\rho \frac{n}{N_A} u_i) &= -\frac{\partial}{\partial x_i}(\rho \frac{n}{N_A} V_{t,i}) + \dot{\omega_n}'' \end{aligned} \tag{2.17}$$

Where,

ρ = density,

u_i = velocity in i direction,

N_A = Avogedgro's number (6.023×10^{23}) [particles/kmol],

$V_{t,i}$ = thermophoretic velocity = $-0.54 \frac{\mu}{\rho} . \frac{1}{T} \frac{\partial T}{\partial x_i}$,

$\dot{\omega}_n''$ & $\dot{\omega}_s''$ = source terms for number density and mass fraction,

μ and T = viscosity and temperature respectively

The soot inception and growth are modelled in terms the soot precursor molecule acetylene (C_2H_2). This model also incorporates the surface reaction with the gas phase chemistry to accurately capture the surface growth and oxidation events. Table 2.2 delineate different reaction steps used in this model.

Table 2.2: Surface reaction steps used in two-equation semi-empirical soot model

Reactions	**Explanations**
i$C_2H_2 \rightarrow 2S_i + H_2$	soot inception
$C_2H_2 + S_i \rightarrow S_{i+2} + H_2$	soot nucleation
$S_i + \frac{1}{2} O_2 \rightarrow S_{i-1} + CO$	soot depletion by oxidation
$nS_i \rightarrow S_{nj}$	agglomeration or aging

Here, S_i represents a soot particle consisting of i carbon atoms. This model assumes that an incipient soot particle consists of 100 carbon particles and a diameter of 1.24 nm. The surface reaction rates are assumed to be functions of temperature (T) and concentration of the reactants. On the other hand, the diameter of the evolving soot is linked with soot mass fractions. The soot diameter is assumed to be independent of the initial soot diameter. This assumption works quite well for turbulent combustion cases where the surface reaction is the dominant process [63].

2.3.3 Detailed Soot Models

The empirical and semi-empirical formulation contain experimental correlations to predict soot formation behavior. The detailed models, on the other hand, use first principle based approach to solve for the soot particle size distribution function (PSDF). Most of the physical processes in soot formation is governed by Brownian collision of the soot particles in gaseous medium. Therefore, the detailed models solve for the Smoluchowski [65, 66] master equation 2.18 for resolving the Brownian collisions of the soot particles. The first term on the right-hand side of the equation represents the number of particles added to the i^{th} size class due to collision among the particles of the smaller sizes. The second term indicates the depletion of i^{th} class particles due to the collision with the other size classes.

$$\frac{\partial N_i}{\partial t} = \frac{1}{2}\int_0^i \beta_{i-j,j} N_j(t) N_{i-j}(t) dj - \int_1^\infty \beta_{i,j} N_i(t) N_j(t) dj \tag{2.18}$$

Where,

N_i = number density of particles of size class i,

$\beta_{i,j}$ = coagulation frequency factor for the entire range of Knudsen numbers [67] ,

∂N_1 = rate of nucleation (N_1) represents the smallest size class.

The collision frequency factor , $\beta_{i,j}$ are defined differently in terms of different ranges of Knudsen number ($K_n = \frac{2\lambda}{d}$) and three different regimes are defined:

1. Free molecular regime [$K_n >> 1$]
2. Continuum regime [$K_n << 1$]
3. Transition regime [$0.1 < K_n < 1$]

Soot formation occurs in some distinct stages. Detailed soot models incorporate different strategies to calculate the evolution of soot number density at those stages. The first stage in soot formation is the nucleation of soot particles. This inception of soot particles occurs due to the collision between two PAHs [68]. Colket and Hall [69] assumed the rate of inception same as the production rate of benzene. Acetylene based nucleation models [70] can also be implemented to simplify the soot model.

The surface growth in soot models occurs due to different heterogeneous surface reactions. While the exact path of reactions is heavily debated, the surface hydrogen-abstraction-acetylene-addition (HACA) mechanism is usually used. The rate of reaction is directly related to the surface area of the soot particles and number of active reaction site available. Steady state approximation can be used to obtain the number density of active radical sites from the number density of all

soot sites. Frenklach and Wang [68] proposed a surface-reaction steric multiplier (α) which represents the ratio of available active radical sites to the total number of radical sites. The value ranges from 0 to 1. Appel et al. [3] proposed an experimental correlation of with temperature and particle size. This correlation was proposed and tested for a pressure range from 0.12 bar to 10 bar for the fuels with C/O ratio varied between 0.6 to 1.3. The HACA [2, 3, 4] surface growth mechanism reaction pathways are described in table 2.3:

Table 2.3: HACA surface reaction pathway [2, 3, 4]

Reactions		$K = AT^n exp(-\frac{E}{RT})$		
		A $[cm^3 mol^{-1} S^{-1}]$	n	E $[kCal/mol]$
1	$S_j + H \Longleftrightarrow S_j^* + H_2$	4.2×10^{13}	1	13
2	$S_j + OH \Longleftrightarrow S_j^* + H_2O$	1.0×10^{10}	0.734	1.43
3	$S_j^* + H \rightarrow S_j - H$	2.0×10^{13}		
4	$S_j^* + C_2H_2 \rightarrow S_{j+2}$ or $S_{j+2^*} + H$	8.0×10^7	1.56	3.8
5	$S_j^* + O_2 \rightarrow S_{j-2}^* + 2CO$	2.2×10^{12}		7.5
6	$S_j + OH \rightarrow S_{j-1}^* + CO$	Reaction probability = 0.13		

Different strategies are found in the literature to model soot in detail, such as:

- **Discrete Sectional Method(DSM):** This method divides the whole particle size distribution function (PSDF) into a number of discrete zones. In general, an exponential distribution is assumed for the PSDF [71]. The soot particles inside a specific section can move to a different section due to the growth or depletion. It is important to account for this intersectional dynamic of the soot particle movement. The sectional source terms are defined to take care of these movement.

- **Method of Moments:** Method of moments (MOM) solves the PSDF by considering moments of the particle size distribution function (PSDF). By taking a finite amount of lower level moments of the PSDF, it gives valuable information about the soot statistics. If we consider, soot to be entirely consisting of carbon particles, the r^{th} moment of the particle number density N_i is defined as equation 2.19 where m_i is the mass of soot particles in a particle of size class i.

$$M_r = \sum_{i=1}^{\infty} m_i^r N_i \tag{2.19}$$

The first two moments have physical interpretation. M_0 gives the total particle number per unit volume and M_1 is the mass of carbon atoms per unit volume. It means soot volume fraction (f_v) can be calculated as $f_v = M_1/\rho_s$. Knowledge of all the moments is equivalent to the complete knowledge of the size distribution itself [72]. But knowing only the first few moments can give us the most practical information about the PSDF.

$$\begin{aligned}
\frac{dM_0}{dt} &= -\sum_{j=1}^{\infty} \beta_{1,j} N_1 N_j \\
\frac{dM_1}{dt} &= 0 \\
\frac{dM_2}{dt} &= \sum_{i=1}^{\infty}\sum_{j=1}^{\infty} ij\beta_{i,j} N_i N_j \\
\frac{dM_3}{dt} &= 3\sum_{i=1}^{\infty}\sum_{j=1}^{\infty} ij^2\beta_{i,j} N_i N_j \\
&\cdots\cdots \\
\frac{dM_r}{dt} &= G_r \text{ [in general]}
\end{aligned} \tag{2.20}$$

By taking the moments of the Smoluchowski equation multiplied with m_i^r and summing over all size classes i, we get the following moment

balance equations 2.20 where, G_r is the coagulation source term. The main difficulty of solving these equation comes from the closure or expressing G_r in terms of a finite number of moments. There are a number of ways to close the moment balance equation: (1) assume a functional form of PSDF [73], (2) quadrature based closure [74], (3) closure by interpolation [4]. The present study uses the method of moment with interpolative closure (MOMIC) [4]. Equation 2.21 represents the general form of moment equation used in MOMIC where R_r and W_r are the source terms for nucleation and surface reaction respectively.

$$\frac{dM_r}{dt} = R_r + G_r + W_r \tag{2.21}$$

The coagulation coefficient, β is non-additive. Therefore, interpolating the coagulation source term, G_r requires functional representation of β for different coagulation regime based on the Knudsen number (K_n). This is done by assuming a grid function of integer order l (f_l) first (equation 2.22). The coagulation source term (G_r) is then expressed with the fraction-ordered grid function (equation 2.23). The fraction-ordered grid functions are determined by Lagrange-interpolation of the integer-ordered grid function as shown in equation 2.24. A reduced moment term ($\mu_r = M_r/M_0$) can be used to represent the integer-ordered grid function $f_l(l = 0, 1, 2, 3, ..)$ which are used to fractional-order reduced moment terms as shown in equation 2.25 for $l = 1$. Thus a total of two interpolation is required to close the coagulaiton source terms. The following set of equations 2.22-2.25 shows the simplified MOMIC formulation for free molecular regime. Detailed description can be found in [4].

$$f_l^{(x,y)} = \sum_{i=1}^{\infty}\sum_{j=1}^{\infty}(m_i + m_j)^l m_i^x m_j^y (m_i^{\frac{1}{3}} + m_j^{\frac{1}{3}})^2 N_i N_j \quad \text{l=0,1,2, ...} \tag{2.22}$$

$$\begin{aligned} G_0 &= \frac{1}{2}K'_{fm}M_0^2 f_0^{(0,0)} \\ G_r &= \frac{1}{2}K'_{fm}M_0^2 \sum_{k=1}^{r-1}\binom{r}{k} f_{\frac{1}{2}}^{(k,r-k)}, \quad \text{r = 2 , 3, ...} \end{aligned} \tag{2.23}$$

$$f_{\frac{1}{2}} = f_0^{\frac{3}{8}} f_1^{\frac{3}{4}} f_2^{-\frac{1}{8}} \tag{2.24}$$

$$f_1 = 2\mu_{\frac{13}{6}}\mu_{\frac{1}{2}} + 4\mu_{\frac{11}{6}}\mu_{\frac{5}{6}} + 2\mu_{\frac{3}{2}}\mu_{\frac{7}{6}} \tag{2.25}$$

- **Stochastic Soot Model:** In deterministic detailed soot models, the exact particle size distribution function can be resolved by taking infinite number of section in DSM or infinite number of moments in MOMIC model. But, the computational effort to do so is not practical. Addition of morphological parameters (e.g. surface volume, surface area to volume ratio, C/H ratio etc.) in the description of PSDF makes the problem high dimensional. A statistical Monte Carlo approach, is therefore, ideal for dealing with such formulation. A stochastic approach utilizes statistical analysis of random soot formation events to predict the true PSDF. .

  SWEEP [75] is a detailed population balance software, which uses this kind of formulation to account for the particulate matters existing in gas-phase domain. It solves the Smoluchowski populaiton balance equation [65] using a Monte Carlo particle method along with the Linear Process Deferment Algorithm (LDPA) [76]. SWEEP is capable of providing large amount of details on structure and composition of soot particles. Apart

from LDPA, an aromatic site model for surface reaction [77, 78] and an improved surface oxidation rate scheme [79] is integrated in the code. The major advantage of using SWEEP over moments or sectional method is that, it can accommodate a large number of internal coordinates which helps in retaining detailed information about the soot aggregate structures and chemical compositions.

CHAPTER 3

POLLUTANT FORMATION IN ECN CONSTANT VOLUME CHAMBERS

3.1 Target Cases

Engine combustion network's (ECN) spray-A combustion chamber is used as the target case for the present study. The combustion chamber is an optically accessible constant volume spray combustion chamber with a volume of 1147 cm^3 as shown in Figure. 3.1. A wide range of data for different exhaust gas recirculation (EGR) condition and initial oxygen percentage is reported by ECN. The experiment starts with burning a premixed acetylene-air mixture using a spark. The hot preburn mixture is then let to cool down. The temperature and pressure both drop during this time. A spray of liquid n-dodecane ($C_{12}H_{26}$) is

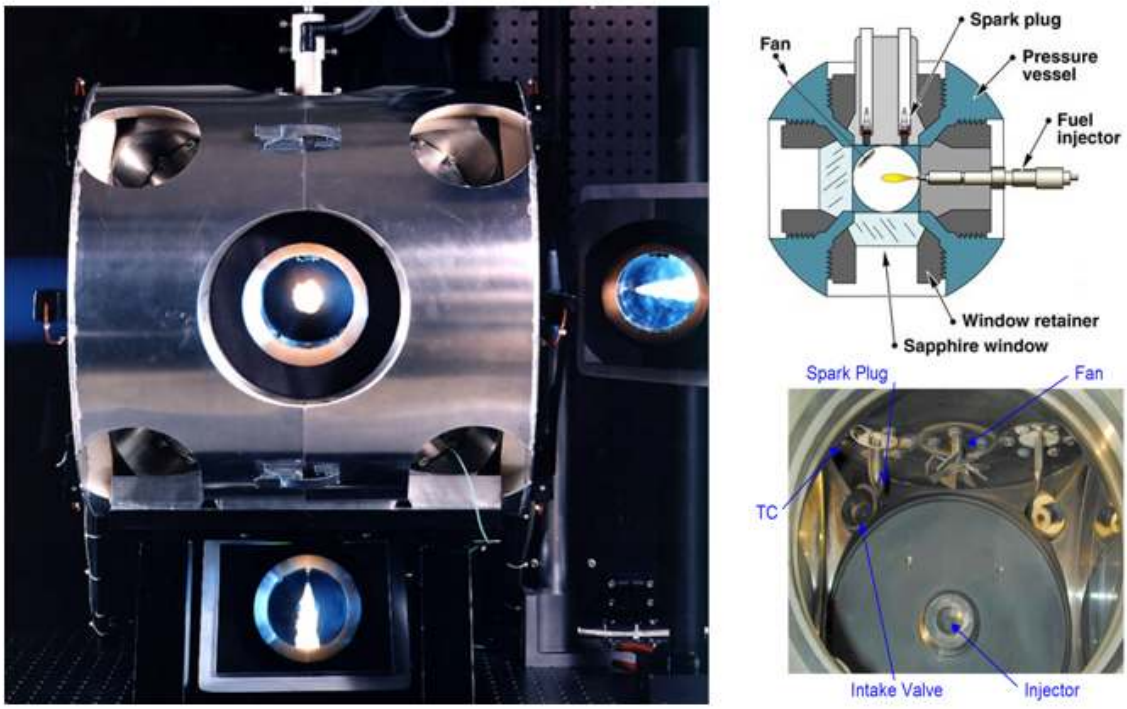

Figure 3.1: ECN Spray-A combustion chamber [8]

injected after the temperature and pressure reaches the desired condition. For the present study, the initial temperature during at the beginning of spray injection is 900 K and the pressure inside the chamber is 6 MPa. The density of the preburn mixture is 22.80 kg/m^{-3}. The preburn mixture contains CO_2, H_2O, O_2 and N_2 which make up the EGR mixture. Three different EGR configurations are considered in the present study. The EGR configurations are denoted in terms of the amount of O_2 content in the EGR mix. A more detailed description of the experimental set up is available at [80].

The injection pressure is 150 MPa and injector orifice diameter is 90 μm. The injection duration is 6 ms. Total mass of fuel injected is 13.77 mg. A recommended rate of injection profile provided by ECN is used for the numerical simulation as shown in Figure 3.2. The present study considers three different EGR configurations with initial oxygen percentages (13%, 15% and 21%). For the non-reacting cases, a 0% O_2 configuration condition is considered while for the reacting cases, the recommended EGR percentages of nitrogen (N_2), water (H_2O) and carbon-di-oxide (CO_2) are considered as provided in [8]. The liquid and vapor penetration lengths in non-reaction condition is used to tune the numerical model used in the present study. The tuned model is then used to run the reacting simulations. Heat release rate, pressure rise, lift off length (LOL) and ignition delay (ID) are validated against the experimental results.

3.2 Parameter and Model Selection

The turbulent flow field is modeled using an unsteady Reynolds-averaged Navier-Stokes (URANS) [81] approach using OpenFOAM-2.3.x CFD toolbox [82]. A pressure-based finite-volume method is used to solve the coupled pressure, momentum, and energy equations with second-order spatial discretization. Effects of turbulent chemistry interaction (TCI) and turbulence radiation

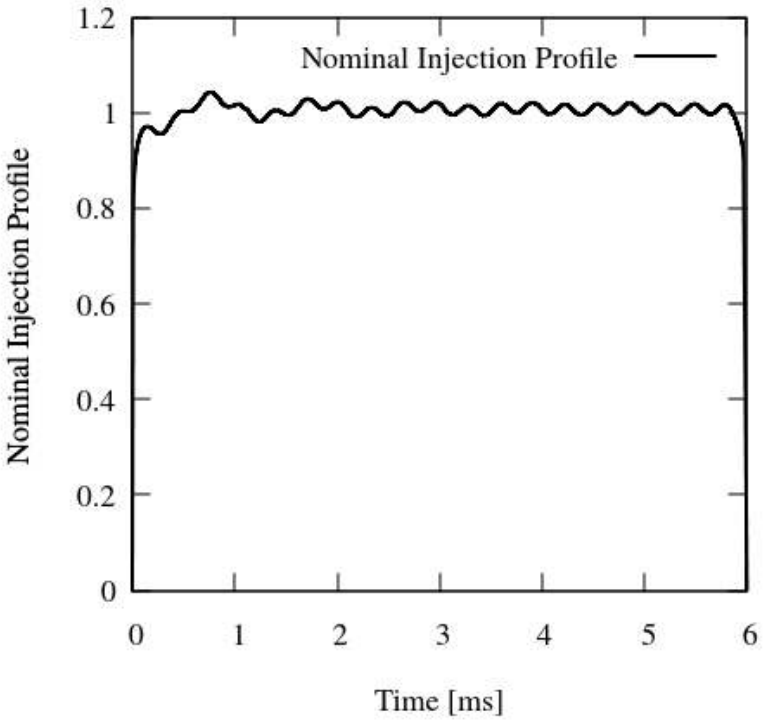

Figure 3.2: Nominal injection rate

interaction (TRI) are not considered in the simulations.

The baseline model parameters used in the present study are summarized in Table 3.1.

The two-equation $k-\epsilon$ turbulence model is used in the present study. The $C_{\epsilon 1}$ constant is increased from 1.44 to 1.55 as recommended by [83]. This modification increases the spreading rate of shear layer of the flow field. The liquid spray is modeled using stochastic Lagrangian-parcel method [84]. The liquid penetration length is dependent on the spray break-up model. Reitz-Diwakar secondary break-up model [1] is used in the current study. The striping constant, C_{s1}, used in the secondary break-up model is set to match the numerical liquid penetration length with the experimental results ($C_{s1} = 9.0$). The vapor penetration length is dependent on the initial turbulence condition. The initial k and ϵ values are chosen to match the experimental vapor penetration

Table 3.1: Summery of numerical models and parameters used in the current study

Physical Process	Formulation	Models	Coefficient Values
Turbulence	URANS [81]	$k-\epsilon$ model	$C_{\epsilon 1}$=1.55[83], C_{μ}=0.09, $C_{\epsilon 2}$=1.92, $C_{\epsilon 3}$=-0.33, σ_k=1.00, σ_ϵ=1.30
Fuel spray	Stochastic Lagrangian Parcel [84]	Blob Atomization and Reitz-Diwakar secondary break-up model [1]	LBU=1.0, C_{bag}=6.0, C_b=0.785, C_{strip}=0.5, $C_{s1} = 9.00$
Gas-phase thermochemistry	Ideal gas mixture	54 species n-dodecane [85]	
Soot		Semi-empirical two-equation model [63] and MOMIC [72, 86]	
Initial k and ϵ			$k = 0.25\ \mathrm{m}^2/\mathrm{s}^2$ [24] $\epsilon = 41\ \mathrm{m}^2/\mathrm{s}^3$ [24]
Combustion		Partially stirred reactor (PaSR) [87]	$C_{mix} = 0.1$

length.

A 54-species, 269-reaction skeletal n-dodecane ($C_{12}H_{26}$) mechanism developed by Yao et al. [85] is used in this study. This mechanism was previously used by Fernandez et al. [24] who showed reasonable agreement with the experimental data. Two different soot models are used in the present study: a semi-empirical two-equation model [63] and method of moments with interpolative closure (MOMIC)[72]. The two-equation model solves two transport equations for soot mass fraction and particle number density. Soot formation is semi-empirically linked with C_2H_2, whereas the soot oxidation pathways include O_2. On the other hand, MOMIC is a detailed soot model which solves for the moments of the particle size distribution function (PSDF) by solving a population balance equation. This model can provide more information about the soot size distribution. MOMIC is expected to provide better estimation of soot formation when used with a sufficiently accurate and detailed chemical mechanism [88]. The soot surface growth in MOMIC follows hydrogen abstraction acetylene (C_2H_2) addition (HACA) pathways [2, 3, 4, 89, 90]. Soot oxidation takes place due to reaction with O_2 and OH. The details of the models can be found in [72, 86].

A fully coupled spectral MCRT radiation solver [30, 91, 92] is used in the present study to account for the gas phase radiation. In PMC, radiation exchange is solved by emitting and tracing a large number of photon bundles or rays. The radiative properties are calculated using a line-by-line (LBL) spectral database obtained from HITEMP2010 database [54]. Three gaseous species (H_2O, CO and CO_2) and soot are considered as participating species. The radiative properties of the soot particles are calculated using a wavenumber-dependent formulation [93]. Spray-phase radiation is based on the multiphase radiation model developed by Roy et al. [30]. The spray droplets are much cooler than surrounding gases and thus considered non-emitting. Due to the lack of

spectrally-resolved radiative property data for dodecane, a gray (i.e., constant complex index of refraction, $n - ik$) assumption is applied to spray droplets. Tuntomo [94] studied the complex index of refraction of n-heptane and n-decane for the mid-infrared range (2-10 μm) and concluded that the refractive index (n) varies by a little while the index of absorption (k) varies wildly with wavelength. In the later studies these outcomes are confirmed by Dombrovsky [95, 96] and the complex index of refraction for Diesel fuel was found to be $n \sim$ O(1.5) and $k \sim$ O(10^{-4}– 10^{-1}) for the mid-infrared range. Following an eralier work [30], the values of the complex index of refraction of the fuel droplets is assumed to be constant at n=1.5 and k= 0.002 in the present study.

As done in [24], a two-dimensional axisymmetric computational domain with a 5° wedge [24] ($1/72^{\text{th}}$ of the experimental domain) is considered as the reaction vessel. The axial and radial dimensions are respectively 108 mm and 58 mm. The entire domain is divided into 12,800 non-uniformly distributed cells. The minimum grid size is approximately 0.25 mm. Figure 3.3 depicts the numerical simulaiton domain used in the present study. Standard wall function is used as the wall boundary conditions. The recommended spray injection rates provided by ECN are used throughout this study. The computational time step is set at 5×10^{-7} s.

3.3 Validation

The numerical model parameters (summarized in Table 3.1) are tuned to match with the experimental liquid and vapor penetration lengths. Since the simulations involve several models, all of which has several tunable parameters, it is impractical to tune each of these models to match each experiment on a case-by-case basis. Therefore, we restricted tuning to only reference nonreacting data such as penetration lengths. Once the tuning is achieved, the parameters are

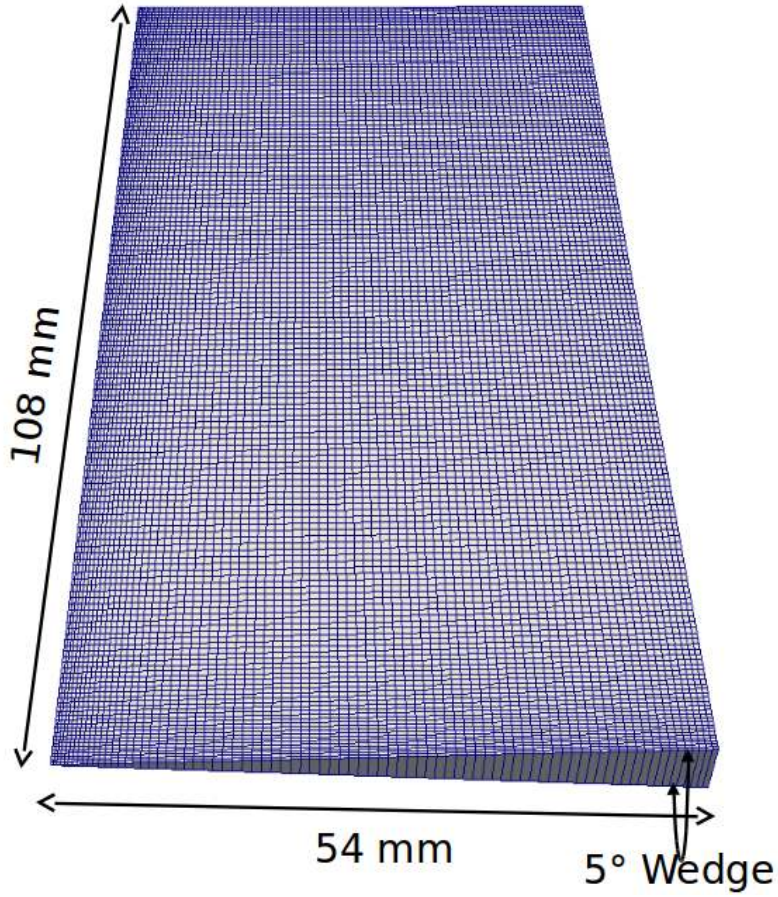

Figure 3.3: Schematic of the simulation domain

fixed for the rest of the study. We then further validated the choice of parameters by comparing simulation results with different reacting characteristics such as the ignition delay (ID), lift-off-length (LOL), heat release rate, pressure rise etc.

3.3.1 Non-reacting Validation: Penetration Length

In the non-reacting cases, fuel spray is injected in the chamber filled with only the EGR gases without any oxygen. ECN defines liquid penetration length as the distance from the nozzle, at which the liquid fuel mass fraction becomes 1%. On the other hand, the vapor penetration length is the distance from nozzle at which the fuel mass fraction becomes 0.1%. Since there is no reaction involved

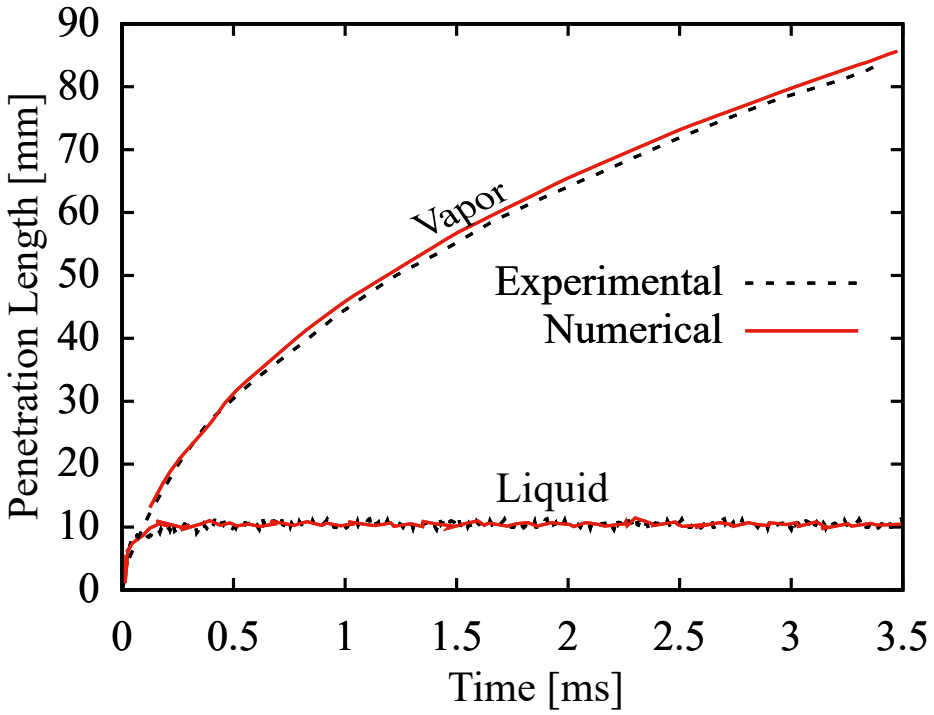

Figure 3.4: Comparison of numerically and experimentally obtained liquid and vapor penetration length in non-reacting condition

(due to the absence of oxygen), the penetration lengths are only affected by the spray break-up parameters and the turbulent mixing configurations. The experiments use acetylene (C_2H_2) premixed combustion to attain the initial conditions required for the self-ignition of the spray. The constant-volume acetylene preburn create a decaying turbulence field, that serves as the initial condition for the spray injection. The vapor penetration length is affected mostly by this initial turbulence field. Therefore, the initial turbulence levels (k and ϵ) are adjusted to match the experimental vapor penetration length. The $C_{\epsilon 1}$ parameter affects both vapor penetration length and lift-off-length (LOL) as discussed in later section. Figure 3.4 compares the liquid and vapor penetration length obtained from the experiments [8] and simulations.

3.3.2 Reacting Validation

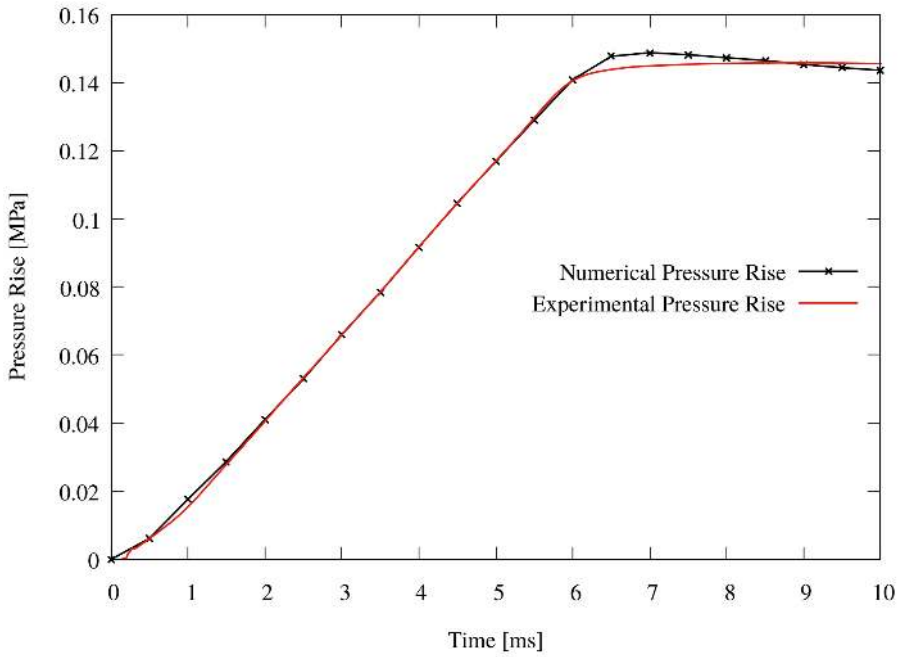

Figure 3.5: Comparison between experimental and numerical pressure rise for 21% O_2 EGR configuration.

The present study uses the tuned numerical model based on the non-reacting cases for the rest of the study without any further modification. Figures 3.5 and 3.6 depict the comparison between experimental and numerical pressure rise and heat release rate respectively. Both of these quantity shows excellent agreement with the experiments. The rise of pressure decreases after the end of injection.

There are several ways to define the ignition delay in a spray combustion system. In this study, a pressure based ignition delay (ID) definition approach is adopted [97, 98]. Accordingly, the ignition delay (ID) period is defined as the instance at which the average pressure in the combustion chamber increases by a nominal 3 kPa amount. This instance indicates the beginning of the second stage of combustion. The chemical heat release rate (HRR) is maximum at this point. Figure 3.7 depicts the ignition delay (ID) for different EGR O_2 percentage cases at

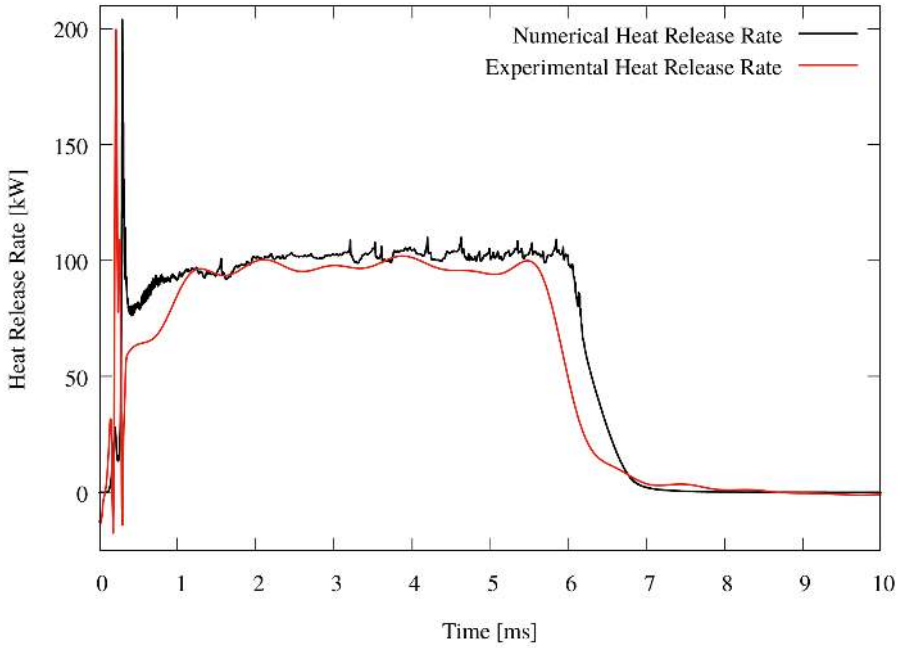

Figure 3.6: Comparison between experimental and numerical heat release rate for 21% O_2 EGR configuration .

900 K. The numerical data follows the same trend as the experiments and the curves are parallel to each other. The ignition delay (ID) period decreases with the increase in EGR O_2 quantity.

The change in the lift-off-length (LOL) with EGR oxygen percentage is shown in Fig. 3.8. The lift-off-length (LOL) is defined as axial location in the quasi-stationary flame where the OH mass fraction becomes 14% of the maximum value in the whole domain. The quasi-stationary flame quantities are obtained by temporal averaging the scalars. In this study, as done by Bolla et al. [99], it is assumed that the reaction domain achieved the quasi-stationary state after 5 ms from the start of injection (SOI). Just like the ignition delay (ID), the lift-off-length (LOL) also decreases with the increasing EGR O_2 quantity. The numerical LOL profiles also follow the experimental LOL profiles qualitatively. The present trends in results are in agreement with similar study conducted by

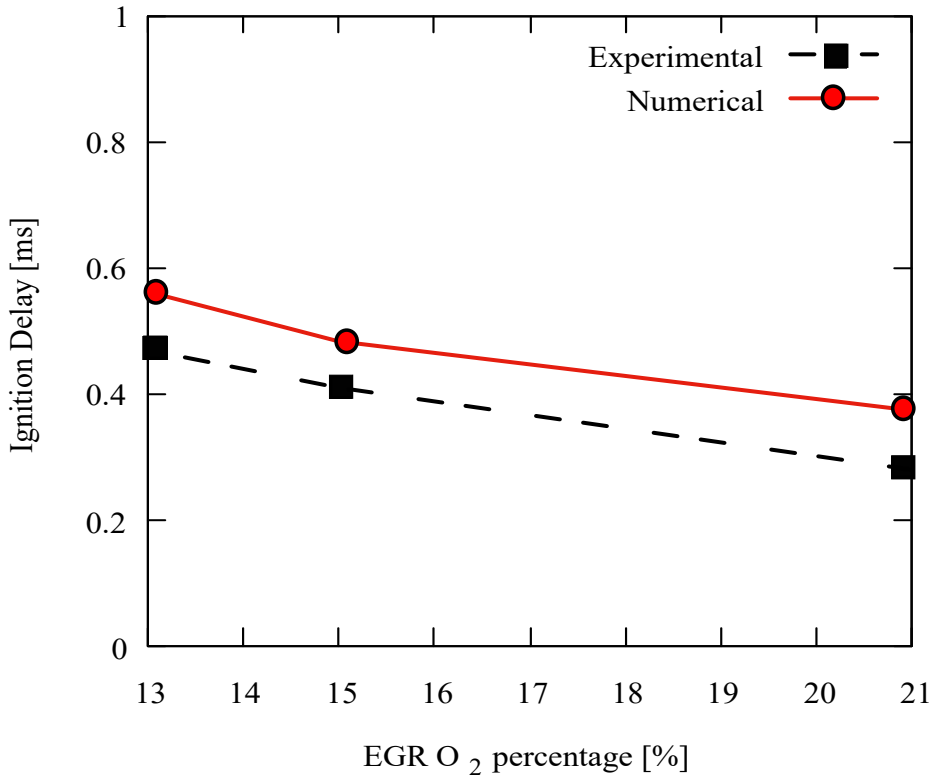

Figure 3.7: Comparison between experimental and numerical ignition delay (ID) with EGR.

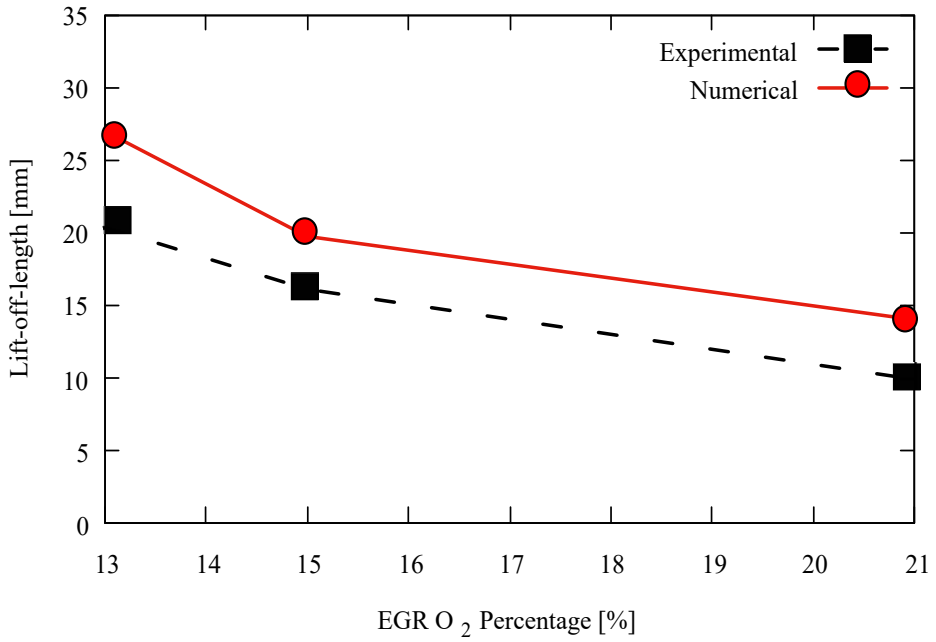

Figure 3.8: Comparison between experimental and numerical lift-off-length (LOL) with EGR.

Fernandez et al. [24].

The discrepancy in the ignition delay (ID) results between the experiments and the numerical simulation can be explained in terms of the choice of chemical mechanism and TCI. As mentioned earlier, the TCI effects are not considered in the present study as we used a partially stirred combustion model. Usually an over-prediction of both ignition delay and ignition delay (ID) occurs when TCI is ignored [99, 100, 101]. Mukut and Roy [102] also showed that choice of chemical kinetic mechanism can significantly alter the flame lift off length (LOL).

The lift-off-length (LOL) also depends strongly on the turbulence characteristics inside the simulation domain. As discussed earlier, the $C_{\epsilon 1}$ parameter in the $k-\epsilon$ turbulence model was changed to 1.55 to match the experimental vapor penetration length. However, this modification increases the lift-of-length. The consistent over-prediction of the LOL is attributed to the limitations of the turbulence model including the the absence of TCI modeling [99, 100, 101] as well as chemical mechanism.

3.4 Effect of Radiation

In this work the gas phase radiation and the spray phase radiation are considered separately. Radiation of the gas phase species and spray droplets may have some effect on pollutant formation behavior due to the local change in temperature because of radiative heat loss.

The inclusion of radiation modeling usually results in lowering of temperature and pressure. Figures 3.9 and 3.10 depict the temporal evolution of the volume-averaged temperature and pressure inside the simulation domain with and without radiation at different EGR configurations. Both the average temperature and pressure decreases with decreasing O_2 percentage in the EGR during the injection period. But, after the injection ends, the rate of cooling

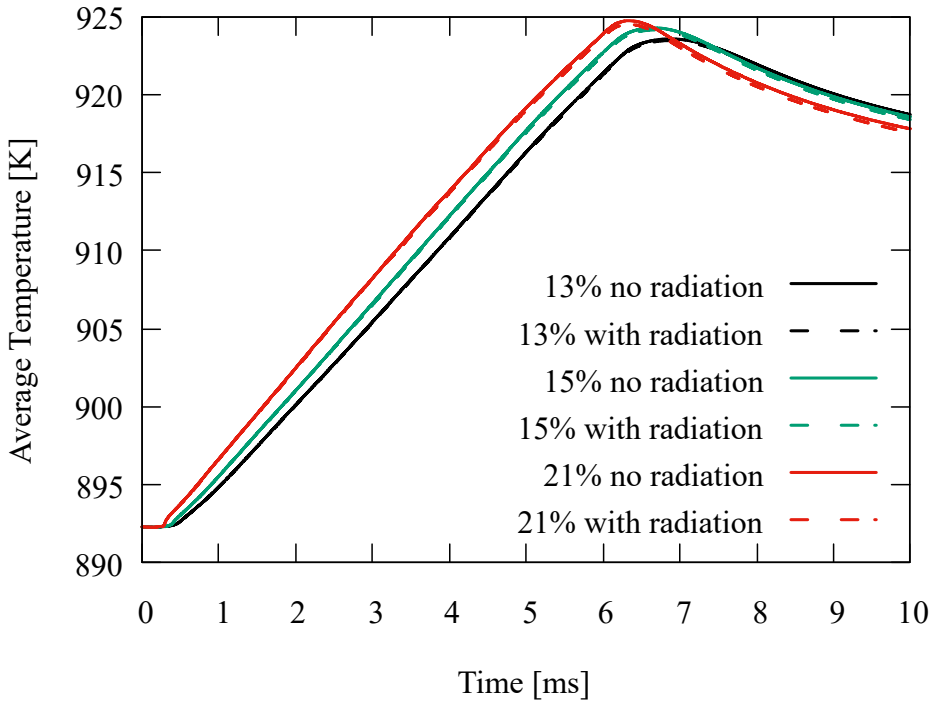

Figure 3.9: Average temperature with and without radiation with different EGR O_2 percentage.

increases with higher EGR O_2 percentage. On the other hand, no noticeable change is observed in the average quantities due to radiation.

Radiation may not noticeably affect the global quantities but it may affect the combustion dynamics by redistributing the temperature field in the simulation domain. The wall emission can also play an important role in near-wall temperature distribution. This change in the temperature field may affect the formation of soot and NO_X throughout the domain. To identify the effect of radiation from different phases (gas and spray), three sets of simulations were performed – without radiation, with only gas-phase radiation (i.e., spray is not participating in radiation), and with both gas and spray-phase radiation (i.e., CO_2, H_2O, CO, soot and spray droplets are all participating in radiation heat transfer). As a representative case, 21% EGR case with MOMIC soot model is discussed here in details. The trends observed are same for other EGR cases.

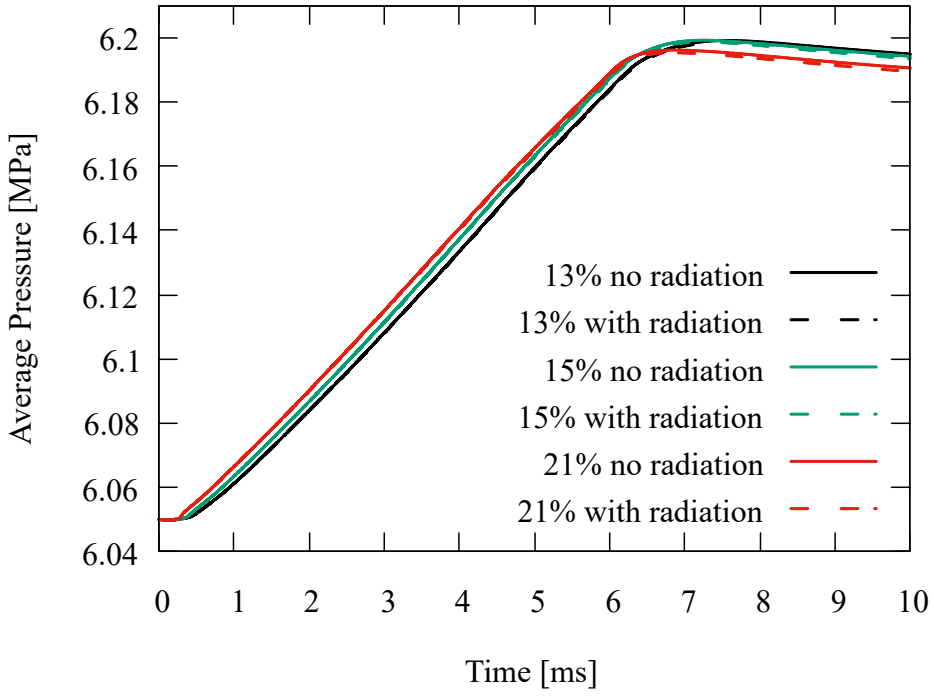

Figure 3.10: Average pressure with and without radiation with different EGR O_2 percentage.

Figures 3.11 (a–c) show the difference in temperature distribution in the simulation domain due to different treatments of radiation at three different instances of time (2 ms, 5 ms and 7 ms) and Fig. 3.11(d) shows the temperature contours with and without radiation models at 5 ms. Noticeable local differences in temperature are observed in these figures due to the multi-phase radiation. A point to note here is that the alternating hot and cold layers seen in the difference plots (Figs. 3.11(a–c) are because of minor shifts in flame front between one simulation and another due to randomness in radiation and spray models and should be ignored while making any inference. In general, gas-only radiation cools down the flame slightly (e.g., mostly hotter regions in Fig. 3.11(c)). However, presence of spray in radiation model makes things highly complex. Although spray droplets are not expected to be heated up directly by radiation in any significant amount [30], their presence may alter local temperature slightly.

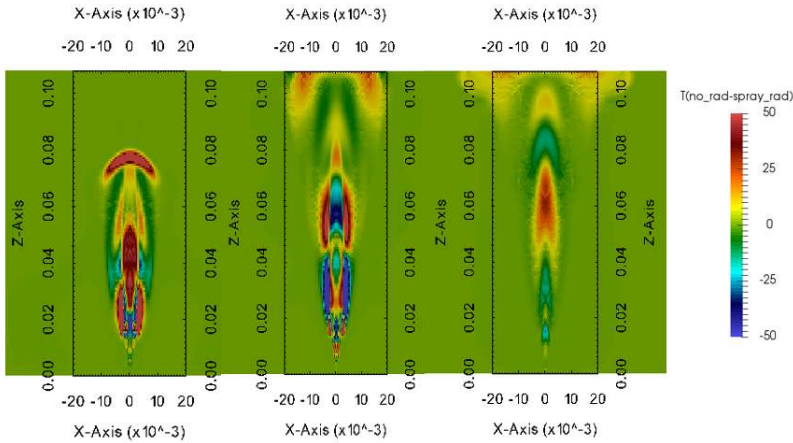

(a) $T_{no\text{-}radiation} - T_{all\text{-}radiation}$

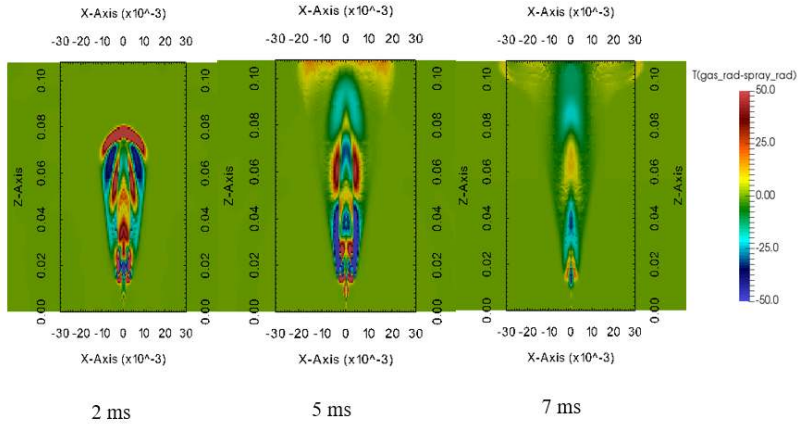

(b) $T_{gas\text{-}radiation} - T_{all\text{-}radiation}$

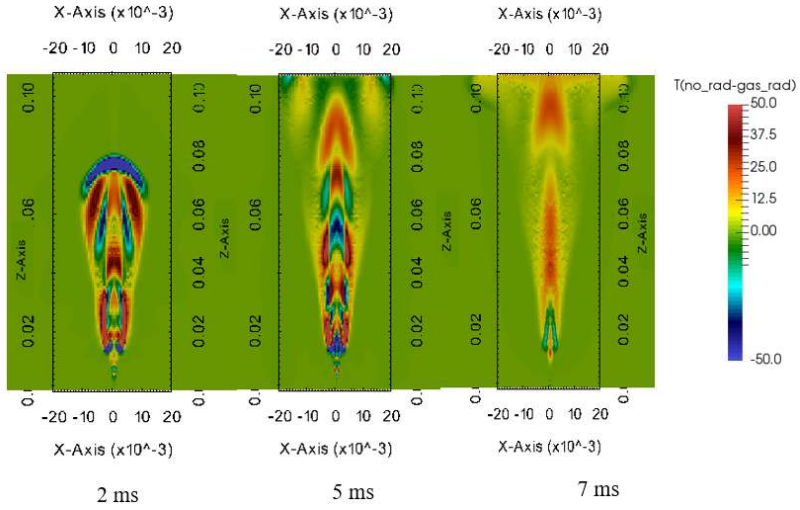

(c) $T_{no\text{-}radiation} - T_{gas\text{-}radiation}$

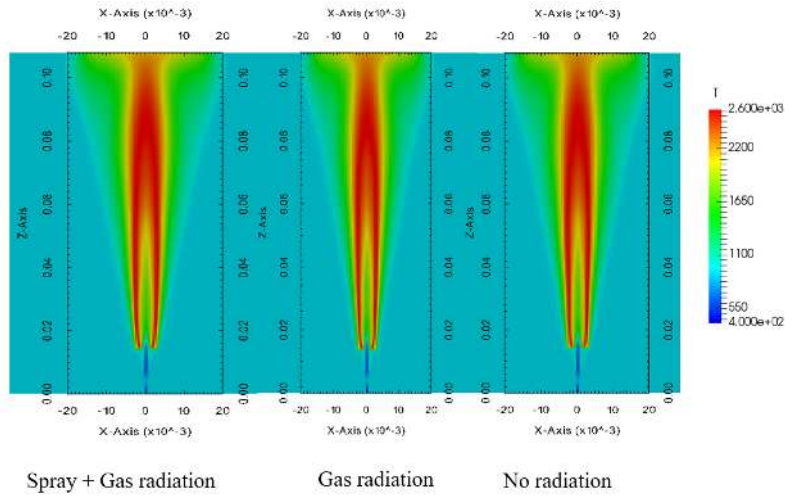

(d) Temperature contours with radiation

Figure 3.11: Temporal evolution of temperature difference due to (a) all (spray and gas-phase) radiation, (b)spray-phase radiation only , (c) gas-phase radiation onlyspray-phase radiation only and (d) temperature contour with and without radiation at 5 ms for 21% EGR O_2 percentage.

Presence of hotter region near the downstream wall at around 5 ms in Figs. 3.11(a-c) indicate that the inclusion of spray in radiation may make the flame marginally shorter, possibly due to localized cooling of gases near the nozzle upstream of the flame. Figure 3.11(b) also indicates that the inclusion spray in radiation makes the flame marginally wider, but also marginally cooler at core post-injection (at 7 ms). It must be noted here that the difference in temperature due to radiation is very localized and small in magnitude, and therefore it does not affect the volume-averaged temperature noticeably as seen in Fig. 3.9.

3.4.1 Soot

Two soot models have been used in this study: a two-equation semi-empirical model and a method of moment of interpolative closure (MOMIC). Figure 3.12 depicts the evolution of soot volume fraction contour with different soot models for 15% EGR case with gas phase radiation at 5 ms. The location and spread of soot formation shows very good qualitative agreement. The peak soot volume fraction prediction from MOMIC is almost double of the two-equation model prediction.

ECN [22] provides the global soot production data with time within an experimental field of view (17.2 mm to 67.2 mm in the axial direction). Figure 3.13 compares the temporal evolution of total soot mass with the experimental data within the experimental field of view for both soot models. Since the simulations are performed with PaSR combustion model, the turbulence chemistry interaction (TCI) cannot be resolved properly. Due to this, the initial variation in the experimental soot profile are not captured by either of the soot models. Using a transported PDF model this trend can also be captured as shown by Fernandez et al. [24]. However, within the scope of this study, both soot models show reasonable agreement with the experimental data.

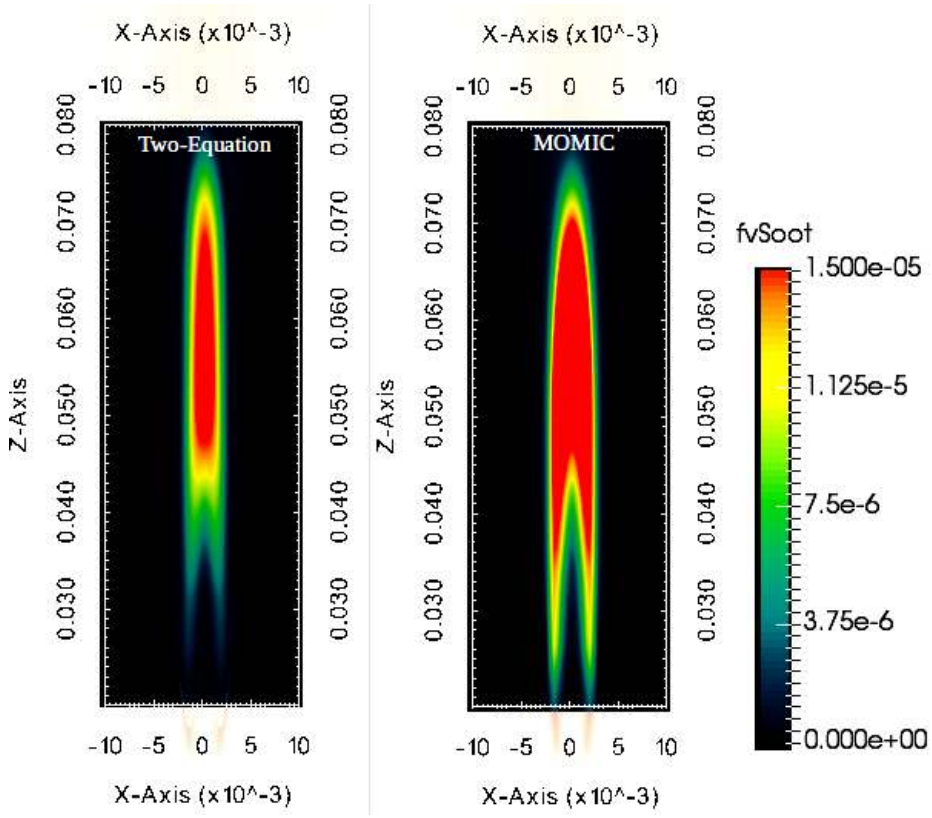

Figure 3.12: Soot volume fraction contours with different soot models for 15% EGR case at 5 ms

From Fig. 3.11, we have seen the effect of spray and gas-phase radiation on the local temperature distribution. Since soot formation is sensitive to the temperature distribution, difference in radiation treatments may affect the overall soot formation. The soot volume fraction contours for the 21% O_2 EGR case with and without spray and gas phase radiation at 5 ms are shown in Fig. 3.14. It is interesting to see that the overall soot production zone remains almost (a marginal reduction can be seen with spray- and gas-phase radiation) same with or without radiation considerations. This is possibly because of the small magnitude of the temperature difference in the soot formation zones. The effect of spray- and gas-phase radiation remains minimal across all the EGR O_2 percentage cases as seen from the global soot production plots in Fig. 3.15. This

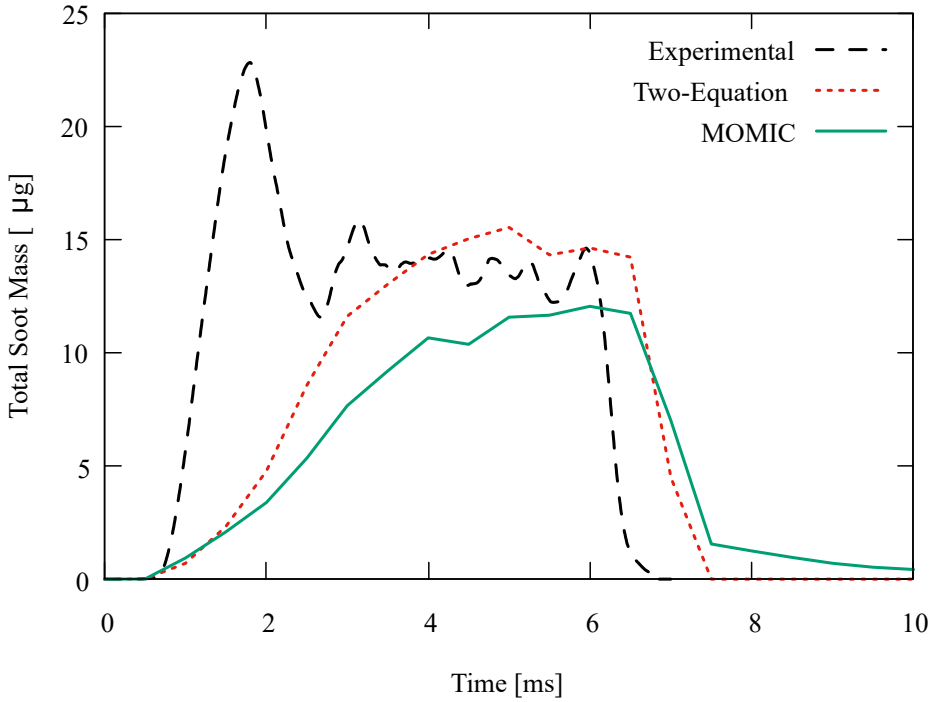

Figure 3.13: Evolution of soot with time within the experimental field of view with different soot models for 15% O_2 EGR case

result is in agreement with the contemporary studies [29, 27].

3.4.2 NO_X

Apart from soot particles, NO_X is another major source of pollutant in internal combustion engines. NO being a major constituent of NO_X, we treat NO as an indicator of overall NO_X behavior in this study. In general, NO formation is a strong function of temperature and mixture fraction but has a weak correlation to pressure inside the combustion chamber [103]. Because of the change in temperature distribution due to the addition of radiation model, NO_X production is affected.

Figure 3.16 demonstrates when and how spray-phase radiation and gas-phase radiation influence NO mass fraction inside the simulation domain. The effect of spray-phase radiation is small compared to gas-phase radiation. The

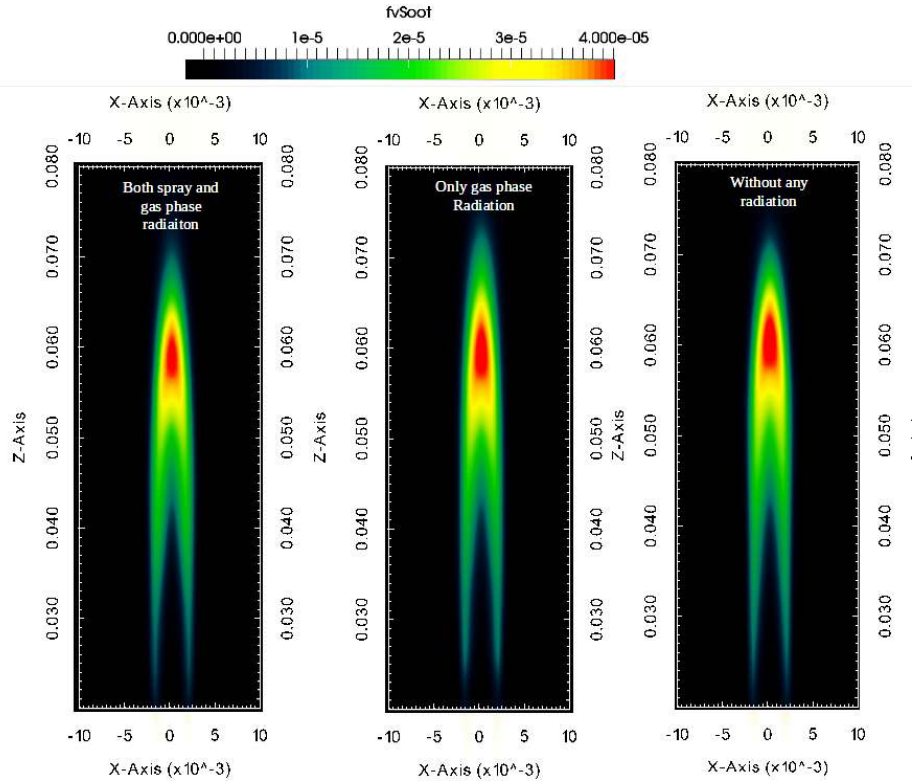

Figure 3.14: Soot volume fraction contours with and without radiation for 21% EGR O_2 case with MOMIC at 5 ms

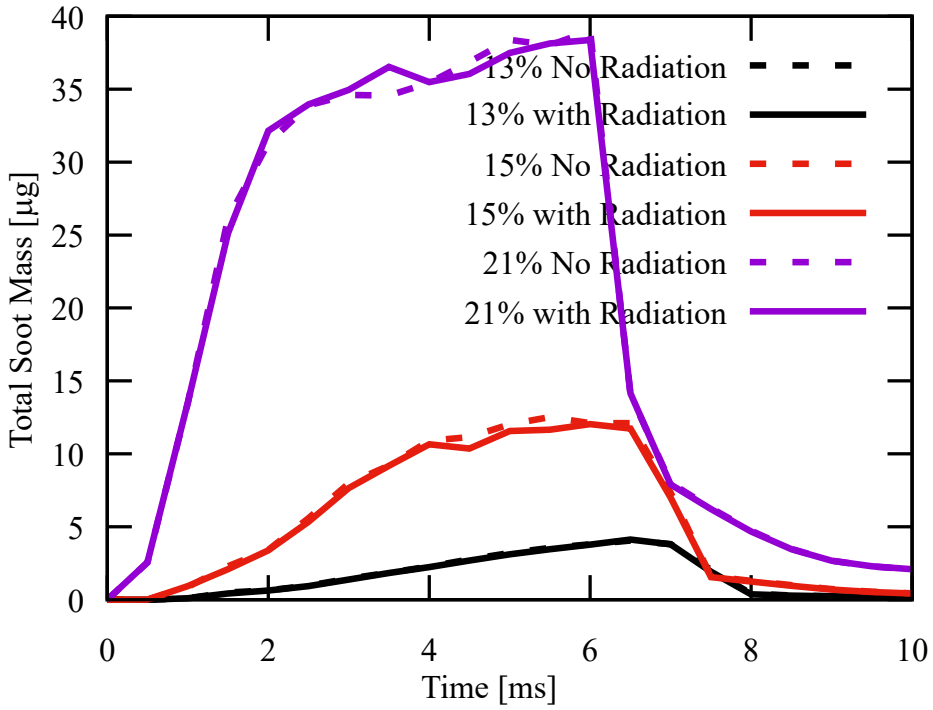

Figure 3.15: Evolution of total soot mass with time for different EGR configurations with MOMIC

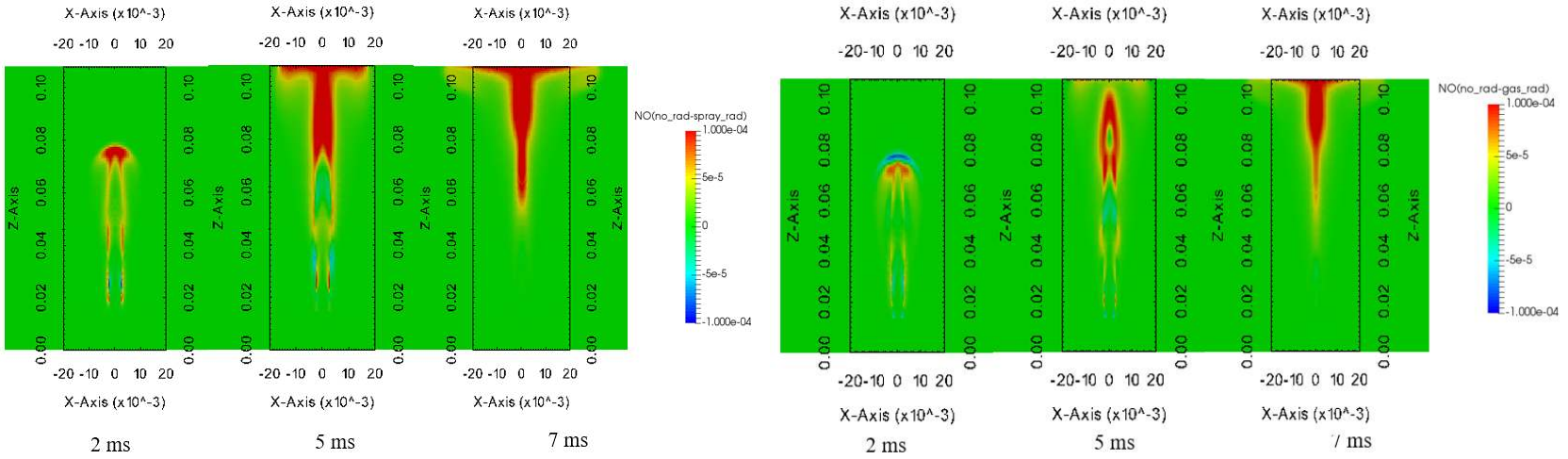

(a) $NO_{no\text{-}radiation}$-$NO_{all\text{-}radiation}$

(b) $NO_{no\text{-}radiation}$-$NO_{gas\text{-}radiation}$

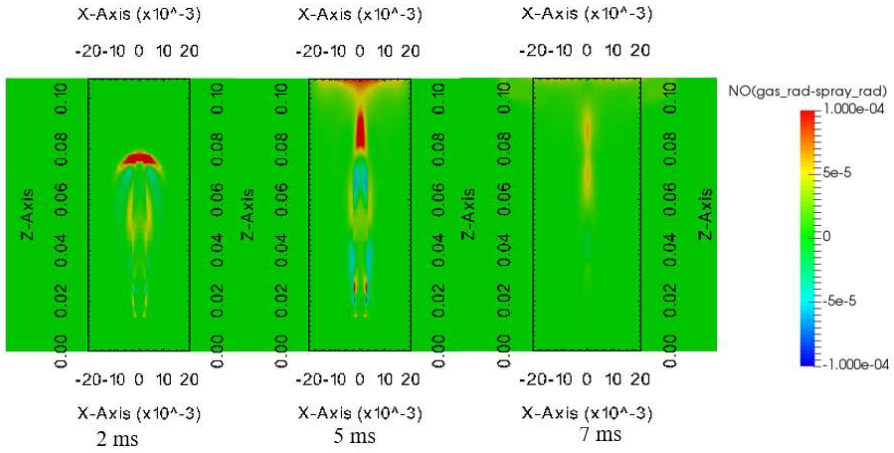

(c) $NO_{gas\text{-}radiation}$-$NO_{all\text{-}radiation}$

Figure 3.16: Change of NO mass fraction with time due to (a) all (spray and gas) radiation, (b) gas-phase radiation only (c) spray-radiation only at 21% EGR O_2 case.

effect of spray-phase radiation decreases after the end of injection as observed in Fig. 3.16(c). On the other hand, the gas phase radiation dominates the core segment of the flame and near the wall. The effect of gas-phase radiation become more dominant with time specially near the wall. From Fig. 3.16, it is evident that, the wall heat transfer plays an important role in NO formation. With the inclusion of radiation model, temperature near the wall decreases due to radiative cooling, leading to a decrease in NO production.

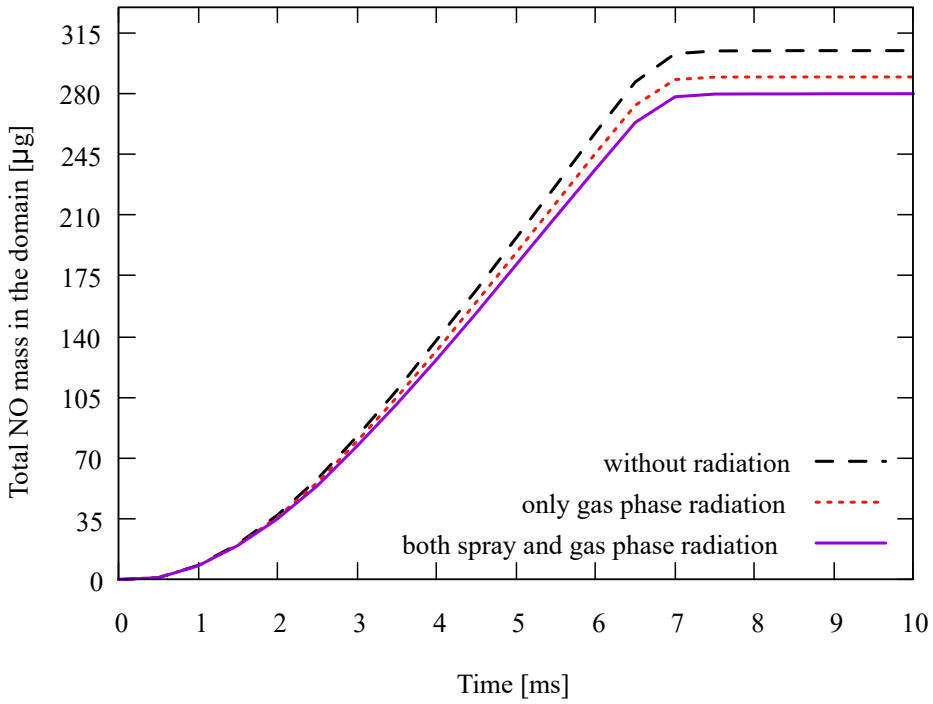

Figure 3.17: Variation of total NO mass in the simulation domain with and without radiation at 21% EGR O_2 case

The localized cooling effect observed with the inclusion of radiation restricts NO formation slightly. Figure 3.17 demonstrates how the global NO production changes with time due to radiation in 21% EGR case. Gas phase radiation plays slightly more important role in reducing the amount of NO (almost 5%) than the spray phase radiation for which the effect is not as impactful

as the gas phase radiation (3.2%).

3.5 Effect of EGR

EGR results in a reduction of temperature which helps reducing NO_X emissions. However, in terms of soot, things are a little different. The extent of EGR influences the intake O_2 amount, i.e. with the increase of EGR the O_2 percentage decreases. The increase of O_2 helps increasing the soot formation but also increases the soot oxidation rate. The link between EGR and soot emission is therefore not quite linear.

3.5.1 Soot

As discussed earlier, two different soot models have been employed in the current study. Figure 3.18 depicts the effect of EGR O_2 percentage on soot formation behavior across both soot models at 5 ms (considering quasi-steady flame). Both soot models show qualitative agreement. However, the MOMIC tends to over-predict the amount of soot for higher O_2 percentage cases and under-predict at lower O_2 percentage cases. Both the location and the amount of soot production are affected by the EGR O_2 percentage. The location of the peak soot volume fraction moves away from the injection nozzle with the decrease of the O_2 percentage in EGR. Also, a steady increase in peak soot volume fraction is observed with the increase of O_2 percentage.

Figure 3.19 depicts the effect of EGR O_2 percentages and different soot models on global soot formation. The results are also compared with the experimental soot data provided by ECN. Although, the two-equation and MOMIC soot model shows qualitative agreement in soot volume fraction profile as discussed in Figure 3.18, there is significant quantitative difference between the soot models. The semi-empirical two-equation model shows surprisingly

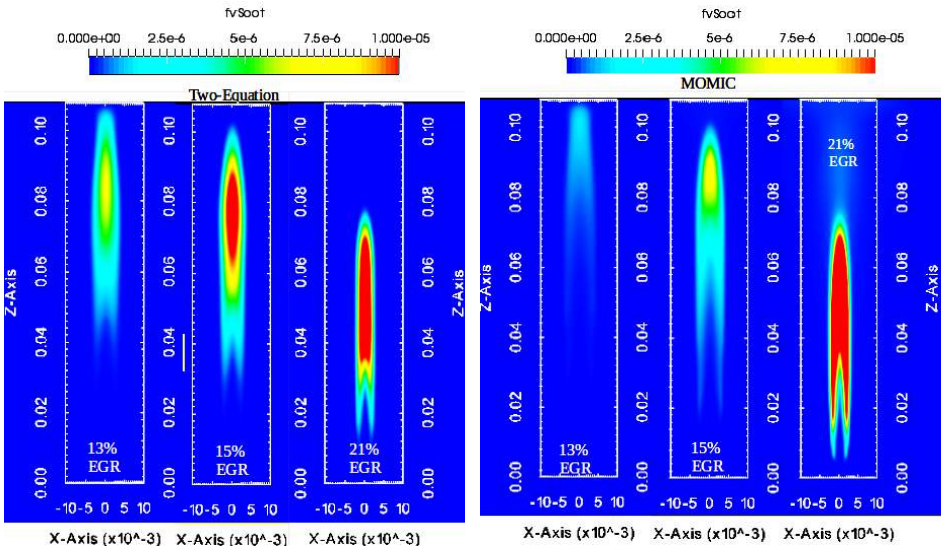

(a) Two-equation model (b) MOMIC

Figure 3.18: Soot volume fraction contours across different EGR using (a) two-equation soot model and (b) MOMIC at 5 ms.

consistent agreement with experimental data in all the EGR cases studied but MOMIC seems to be very sensitive towards the amount of O_2 in the EGR. O_2 plays an important role in the surface growth reactions during soot formation [104, 4] as well as in oxidation of soot particles. The sensitivity of the MOMIC with O_2 percentage in EGR can be partially attributed to this two-way role of oxygen. Since, the semi-empirical two-equation model uses empirical correlations to account for surface growth, no strong sensitivity is observed in two-equation result. It has also been shown in other studies that MOMIC in general tends to be more sensitive to gas-phase chemistry than semi-empirical model [88]. It should be noted that, a better match with experimental data with the semi-empirical model than the detailed MOMIC is somewhat fortuitous as this study does not take into account turbulence-chemistry and turbulence-radiation interaction (TCI and TRI) effects rigorously. With TCI and TRI, along with a better chemistry with aromatics, MOMIC has been shown to produce a better match in Spray-A in the literature [24].

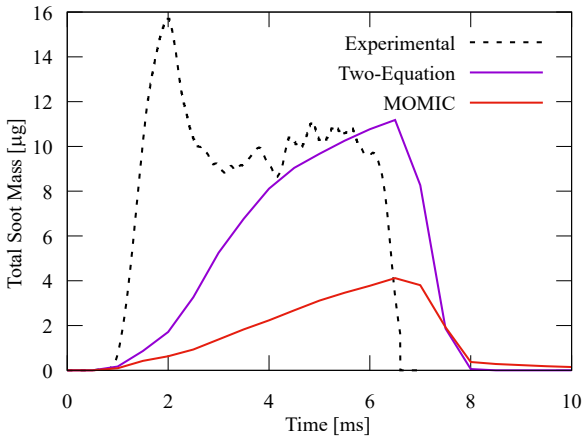

(a) EGR 13% O_2

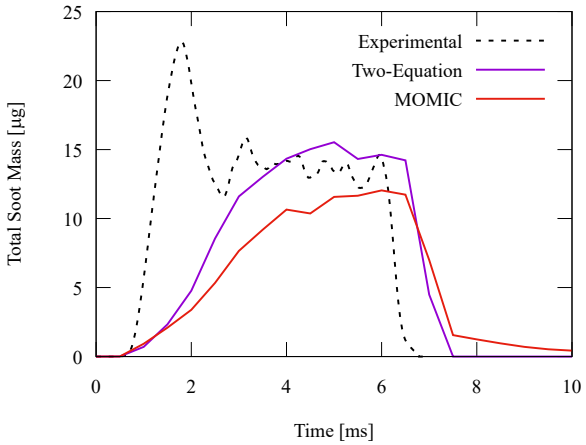

(b) EGR 15% O_2

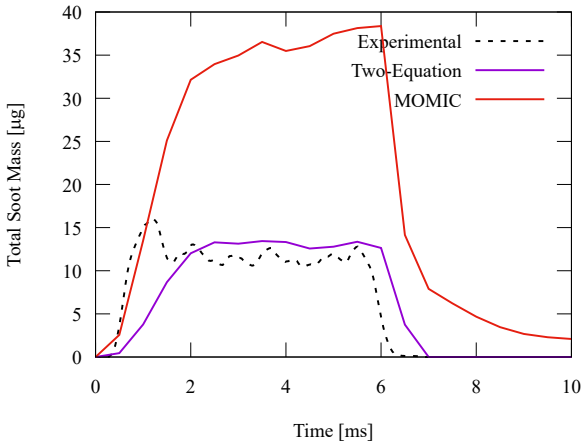

(c) EGR 21% O_2

Figure 3.19: Effect of EGR O_2 quantity and soot models on global soot formation characteristics in the experimental field of view.

3.5.2 NO_X

As discussed earlier NO formation is very strongly related to the temperature and mixture fraction of the flame in the combustion chamber[103]. With the increase of EGR, the O_2 % in the gas mixture decreases and with that the temperature inside the combustion chamber also decreases and so does NO.

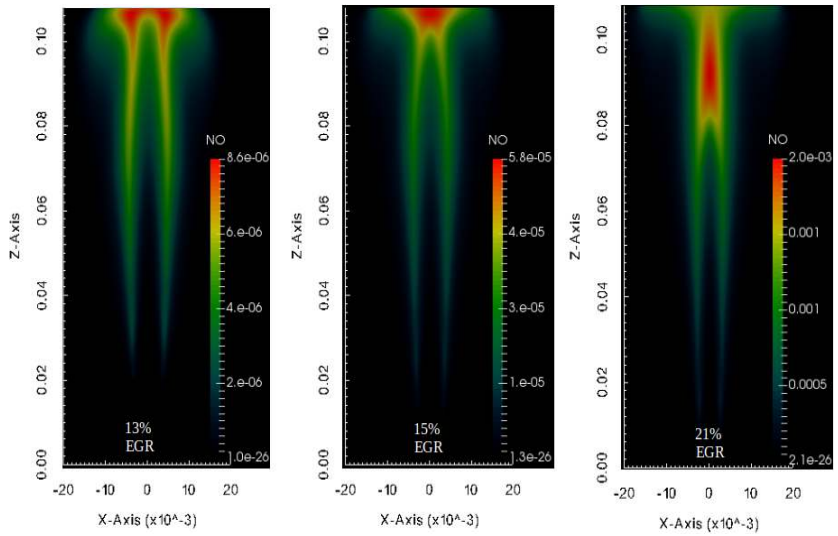

Figure 3.20: NO mass fraction contours for different EGR conditions at 5 ms

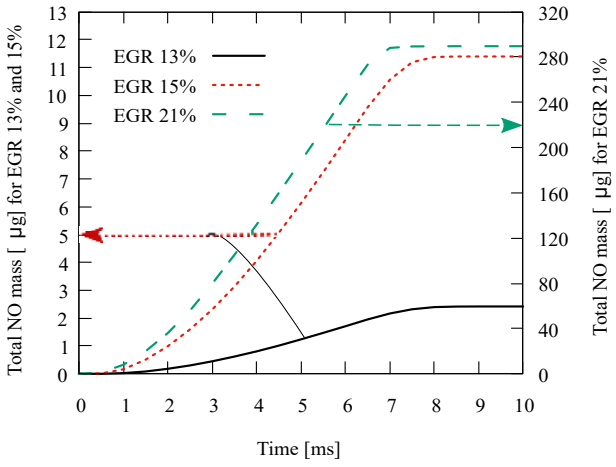

Figure 3.21: Effect of EGR on the total NO mass produced in the simulation domain (13% & 15% in left axis and 21% in right axis)

Figure 3.20 illustrates the comparison of NO formation behavior with different EGR O_2 percentage at 5 ms. The maximum value in the contour plots are kept same as the maximum NO mass fraction in individual cases. From 13% EGR to 15% EGR O_2 case, the peak NO mass fraction increases by an order of magnitude. Two orders of magnitude increase is seen between 21% and 15% EGR O_2 content. With the decrease in the O_2 content, the wall radiative heat transfer effects can also be observed. The NO profiles for 13% O_2 EGR is much wider than the 21% case near the wall. The global effect of EGR on overall NO production is shown in Figure 3.21. The total NO mass produced in 21% O_2 EGR case is much higher than the other two. Figure 3.21 clearly indicates that the NO emission can be significantly reduced with the increase of EGR (lower O_2).

3.6 Summary

A systematic sensitivity study has been conducted on engine combustion network's (ECN) high pressure spray-A combustion chamber. Different aspect of soot and NO_X formation is investigated with three different EGR O_2 configurations and with the inclusion of spray and gas phase radiation separately. An in situ PMC-LBL multiphase radiation solver is coupled with two-different soot models to observe the effect of radiation on overall soot formation.

Some key findings of the study is listed below:

- The effect of radiation is negligible on the average temperature and pressure of the spray-A combustion chamber.
- Effect of spray and gas phase radiation on soot is minimal in ECN spray-A combustion chamber.
- As EGR O_2 percentage increases, the peak soot volume fraction also increases.
- MOMIC shows significant sensitivity towards the EGR O_2 concentration.

- Both Radiation and EGR has noticeable effect on NO production. Increase in EGR O_2 percentage increases NO. Radiation causes change in local temperature distribution, which in turn reduce NO production throughout the domain.
- The gas-phase radiation has more effect on NO formation than the spray-phase radiation.

CHAPTER 4

EVOLUTION OF SOOT MORPHOLOGY IN HIGH-PRESSURE SPRAY COMBUSTION

4.1 Methodology

The size and morphology of the engine-out soot have significant effect on the environment. The effect of EGR and radiation on global soot yield has been described in the previous sections using both a two-equation model and a MOMIC soot model. The semi-empirical two-equation soot model does not resolve size-related information in great detail. MOMIC, on the other hand, follows evolution of soot from first principle and can resolve the moments of the PSDF. MOMIC accounts for four fundamental physio-chemical processes involving soot – nucleation, coagulation, surface growth (following the HACA [2] pathway), and oxidation [4, 72, 88]. In this section, we present some global information related to the soot particle size distribution obtained from MOMIC. It is important to note here that, the current MOMIC formulation assumes spherical soot particles and the gas-phase chemical mechanism does not contain any PAH. Therefore, the analysis presented here may lack some details in soot morphological information. But the information extracted are still worth looking as they reveal some important qualitative information.

In the present study, the probability density function (PDF) of soot particle diameter is investigated in detail. As discussed earlier, MOMIC formulation gives the soot particle diameter and number density of the soot particle inside the simulation domain.From these information, the frequency distribution of the soot particle diameter can be calculated. The soot diameter distribution is then classified into similar sized bins and number of soot particle in each bin is counted. This gives us the PDF of soot particle diameter inside the domain.

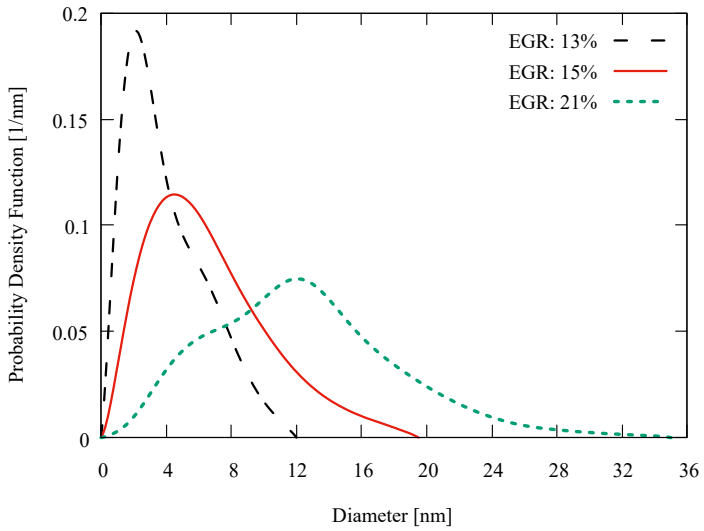

Figure 4.1: PDF of soot diameter with different EGR configurations at 5 ms

4.2 Evolution of Soot Morphology with Location and Time

Since the spatial distribution of temperature varies with different EGR configurations, the soot particle distribution also varies. The way this soot particle distribution changes with time and location inside the combustion chamber gives us valuable information about the physio-chemical processes that governs soot formation. The following section will discuss the temporal and spatial variation of soot particle size distribution across different EGR configuration.

4.2.1 Effect of EGR

Figure 4.1 depicts the global probability density function (PDF) of the soot particle diameters in different EGR cases considering the entire chamber at 5 ms. The time instance of 5 ms is chosen because it represents the quasi-steady state of the simulation [99]. Looking into this quasi-steady state results helps us understand the global effect of EGR on soot statistics. The diameter distributions become wider with the increasing O_2 percentage which indicates a wider range of particle diameters in the simulation domain. The mean of the soot diameter

increases with the increase of EGR O_2 percentage. Higher amount of O_2 in the EGR mix invokes a more favourable condition for growth of soot particles. The 21% O_2 configuration almost tripples the maximum soot diameter from 13% O_2 EGR case.

4.2.2 Temporal Evolution of Soot

The evolution of the diameter of the soot particles with time also gives us important insights about the evolution of soot. In the cases under consideration, the simulation is run for 10 ms while the spray lasts for 6 ms. Figures 4.2 – 4.4 show the changes of diameter PDF with time inside the combustion chamber for 13%, 15% and 21% O_2 cases respectively. For clarity, the plots are divided into two separate parts, (a) during spray injection and (b) after the end of spray injection. The total soot mass and number density in the simulation domain on a particular time is also included in the corresponding legends. The bimodal nature of the PDF profiles show the balance between formation, coagulation, surface growth, and oxidation during different phases of combustion. Only nucleation and coagulation affect the number density of soot – nucleation introduces incipient soot particles, whereas coagulation reduces number of soot particles without affecting soot mass. On the other hand nucleation and surface growth introduce new mass to soot, while oxidation reduces mass of a soot particle. The first peak is indicative of mostly the incipient soot particles. The second peak represents the previously formed soot particles which are going through a balance between coagulation, surface growth and oxidation. Depending on the extent of different phases of soot formation, the shape of the diameter PDF can change and because of that, the width and existence of the two peaks may also vary.

During the spray injection, all the cases under consideration show a rapid increase of soot mass and number initially up to 2 ms as seen from Figs. 4.2(a),

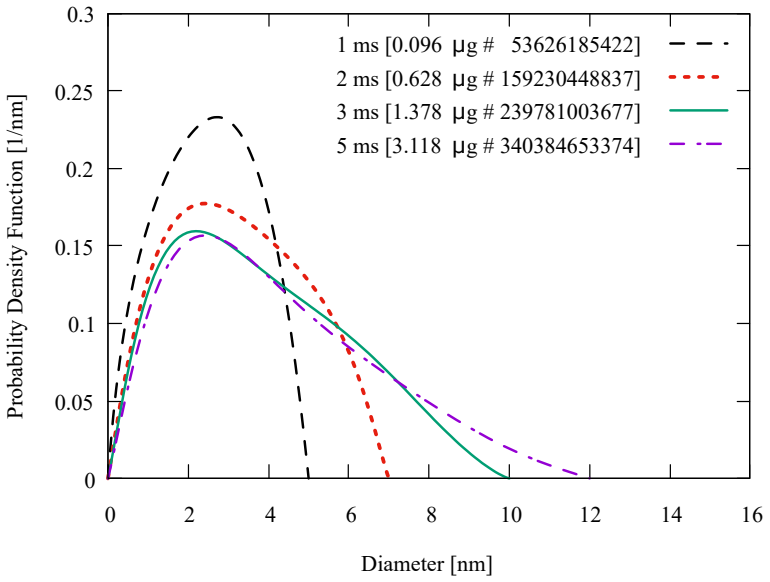

(a) During spray injection

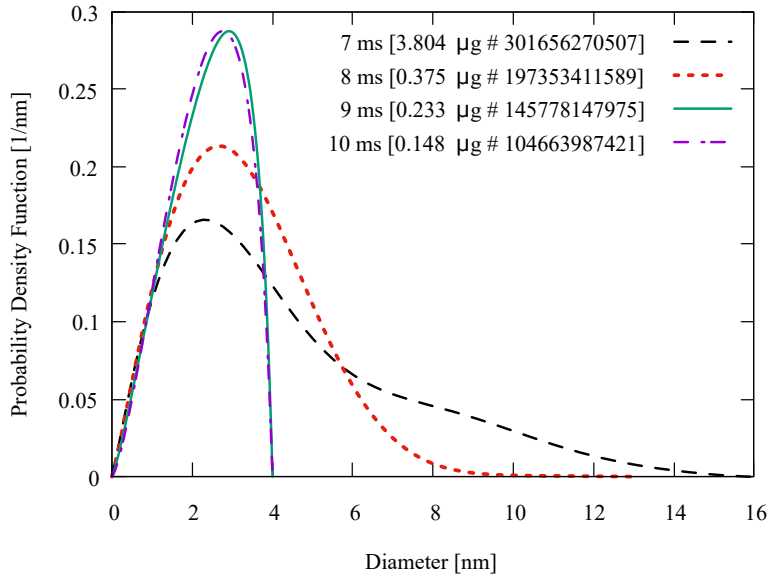

(b) After spray injection

Figure 4.2: Evolution of PDF of soot diameter with time at 13% O_2 EGR case: (a) during injection, (b) after the end of injection

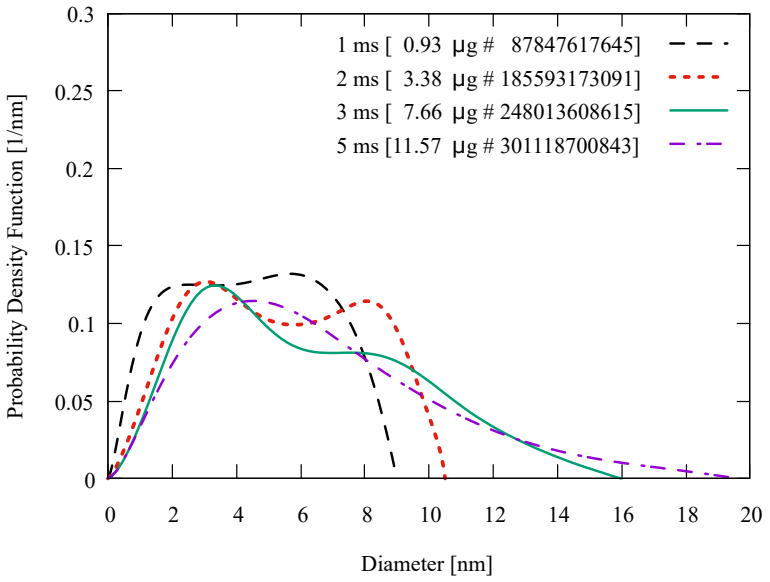

(a) During spray injection

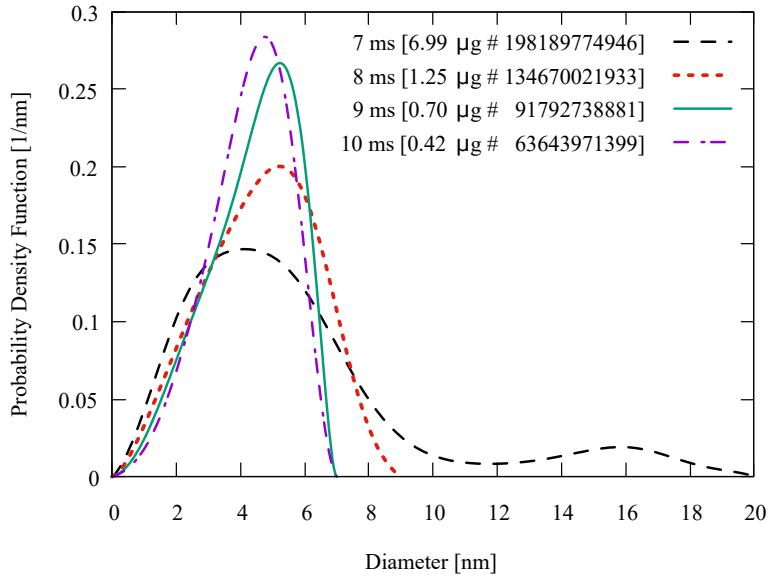

(b) After spray injection

Figure 4.3: Evolution of PDF of soot diameter with time at 15% O_2 EGR case: (a) during injection, (b) after the end of injection

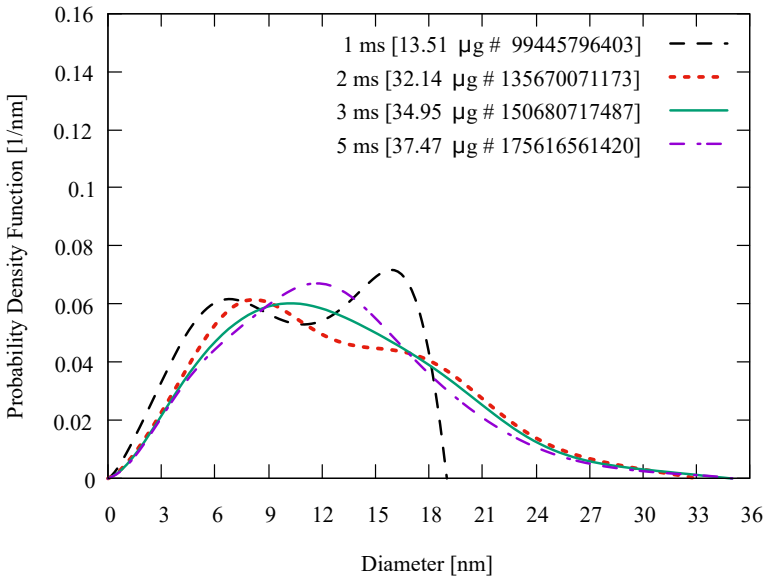

(a) During spray injection

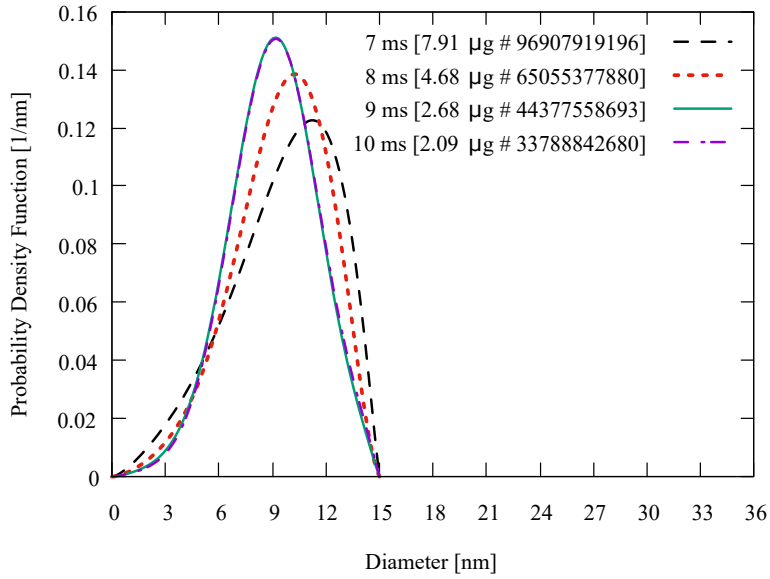

(b) After spray injection

Figure 4.4: Evolution of PDF of soot diameter with time at 21% O_2 EGR case: (a) during injection, (b) after the end of injection

4.3(a) and 4.4(a). This indicates rapid nucleation in the beginning of each case. After that, the total number of soot particles becomes more or less steady until the end of spray injection. During this period the soot mass continues to increase. This increase in soot mass with a small change in total number of soot particles represents rapid surface growth during this period. The soot diameter PDFs keep getting wider until a balance between surface growth and oxidation kicks in. After the end of spray injection, the amount of soot decreases rapidly due to oxidation as seen from Figs. 4.2(b), 4.3(b) and 4.4(b). The effect of nucleation increases with the decrease of O_2 percentage in the combustion domain. For the 13% O_2 EGR case there is essentially one single peak that is visible during the entire 10 ms. Although the diameter profile widens from 3 ms to up to 8 ms due to coagulation and surface growth, these phenomena are not strong enough to produce a distinct second peak. The peak of the PDF remains close to 2 nm indicating strong effect of nucleation during initial stage (up to 2 ms) and oxidation during the later stage (8 ms to 10 ms). For 15% O_2 EGR cases, we see a co-existence of both mature (larger diameter) and newly-formed (smaller diameter) soot particles even after the injection ends at 6 ms (until 7 ms). The presence of a second peak indicates increasing importance of surface growth and coagulation. For 21% O_2 case, the bimodal shape is only visible during initial stage (up to 2 ms). Beyond that the surface growth essentially shifts the peak towards larger particles (2 ms to 5 ms). The oxidation is strongest in this case resulting in quick elimination of large particles immediately after the end of injection (Fig. 4.4(b)). All cases show a very similar soot diameter PDF between 9 ms and 10 ms which indicates a slow-down of physio-chemical activities related soot. This is because by this time most of the soot has oxidized from the domain as also seen in Fig. 3.15. From Figures 4.3 and 4.4 we observe two distinct trend with time. In the first half, coagulation and surface growth becomes dominant

over soot nucleation as seen by shift of diameters to larger values. In the later half, oxidation becomes more prominent over surface growth as seen by a decrease in larger diameter particles. This eventually decreases the diameter of soot particle and produces a narrow diameter PDF with time.

4.2.3 Spatial Evolution of Soot

The axial variation of the soot diameter gives us important insights about the maturity of the soot particles along the direction of the spray. Figure 4.5 depicts the axial variation of the spatially-averaged (along the horizontal plane) diameter PDF in 21% O_2 EGR configuration at three different axial locations (36 mm, 45 mm and 60 mm). The colored points in the figure represents the planar mean of soot diameter at these locations as measured by Cenker et al. [9]. The numerical planar-averaged diameter is within 30% of experimental data of the experimental data. The locations are chosen to represent different segments of the soot formation zone. The 36 mm location marks the start of the soot formation zone and 60 mm location represents the peak soot formation zone as seen in Figure 3.14. The bimodal nature of the diameter PDFs are more pronounced in the downstream than the upstream locations. The magnitude of the peaks decrease and the shape of the profiles shifts towards larger particles at the 60 mm location. This points to the dominance of surface growth and coagulation at this location.

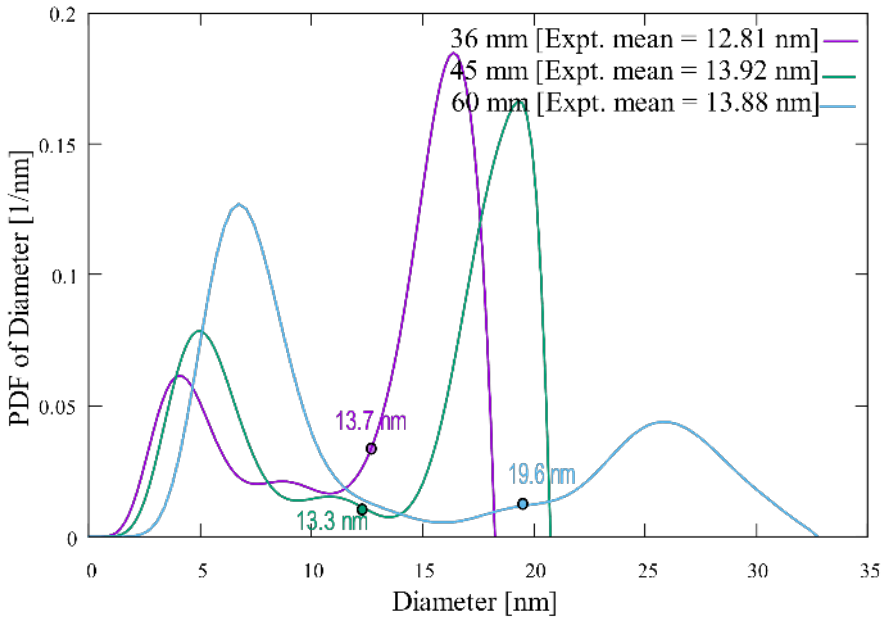

Figure 4.5: Planar-averaged PDF of soot diameter for 21% O_2 EGR configuration and experimental mean diameter [9] (vertical lines) at different axial locations

4.3 Summary

This chapter presented a detailed discussion about how the soot particle diameter statistics changes with three different EGR configurations. As noted earlier, MOMIC assumes only spherical soot particle and because of that the diameter of soot particles contains the full morphological information. Both temporal and spatial variation of soot diameter PDF is discussed and compared with the available experimental results.

Some key findings are listed below:

- The soot diameter distribution is significantly affected by the EGR configuration. The mean soot diameter increases with the increase in EGR O_2 percentage.
- The PDF of soot diameter becomes wider with the increase in EGR O_2 percentage. It means that, higher amount of O_2 in the EGR mix provides

more favorable condition for soot formation.

- Coagulation and oxidation starts to dominate only afer the end of spray injection. During the spray, soot evolution is dominated by nucleation.
- Surface growth and coagulation becomes dominant downstream, away from the nozzle.

CHAPTER 5

CONCLUSION

A comprehensive numerical study has been conducted on ECN spray-A combustion chamber with detailed chemistry, detailed radiation solver, and different soot models for different EGR O_2 concentration. The numerical results are validated with liquid penetration length, vapor penetration length, ignition delay (ID), lift-off-length (LOL), chemical heat release rate (HRR), pressure rise and global soot mass. The soot and NO_X formation behaviors are carefully investigated to see how they change with radiation and EGR configurations. The soot diameter distributions are also examined and compared with the experimental data.

A detailed multiphase radiation model is used to investigate the effect of radiation in ECN spray-A combustion chamber. It is found out that radiation has minimal effect on the average temperature and pressure distribution for spray-A configuration. Some local variation in the temperature field is observed due to spray and gas phase radiation but these variations are not significant enough to globally effect the soot formation characteristics. EGR, on the other hand, has a significant effect on soot formation. The peak soot volume fraction increases with the increase in EGR O_2 configuration. Between the two soot model used, MOMIC shows significant sensitivity with the amount of O_2 in the EGR mix.

Both radiation and EGR affects NO production in the simulation domain. Radiation causes change in local temperature distribution, which in turn reduce NO production throughout the domain. Both spray and gas phase radiation helps reducing the global amount of NO in the domain. The effect of gas phase radiation is more significant than spray phase radiation.

The spatial and temporal distribution of soot particles are investigated in the present study. Both location and diameter distribution of the soot particles are affected by EGR. The mean soot diameter increases with EGR O_2 percentages. The diameter distribution becomes wider with the increase of oxygen percentage in EGR. Surface growth and coagulation becomes dominant downstream, away from the nozzle. Oxidation starts to dominate only after the end of spray injection.

CHAPTER 6

FUTURE WORK

In the present study, a systematic investigation has been conducted to see the sensitivity of soot and NO_X formation with EGR, radiation and different soot models. A Reynolds average simulation framework is used along with a photon Monte Carlo line by line (PMC/LBL) multiphase radiation solver. Due to the use of the RANS framework with a partially stirred reactor (PaSR) model, the current study failed to show the turbulent chemistry interaction (TCI) and turbulent radiaiton interaction (TRI). To get the full picture of soot formation and its interaction with turbulence and radiation, future studies should be conducted using transported PDF (tPDF) combustion models. The use of a detailed PAH chemical mechanism is also advised to get the full advantage of MOMIC soot model.

The statistics of the soot particles inside the combustion chamber is also investigated in the present study based on the soot particle diameter distribution. The MOMIC soot model used in this study assumes spherical soot particles which looses most of the morphology related information. A major area of improvement is to improve the soot model to accompany more morphology related information. A more rigorous soot model can be used to look into the morphological evolution of soot particles. Some preliminary studies have been conducted with a stochastic soot model software: SWEEP [78, 77, 77, 75, 76]. This model employs a statistical approach to model soot and carry additional morphological information for soot particles, e.g. fractal dimension, C/H ratio, surface area , mobility diameter, surface to volume ratio etc. Figure 6.1 shows the numerical rendering of soot particle in ECN spray-A combustion chamber for 15% EGR O_2 configuration at 36mm axial location and its evolution with time in

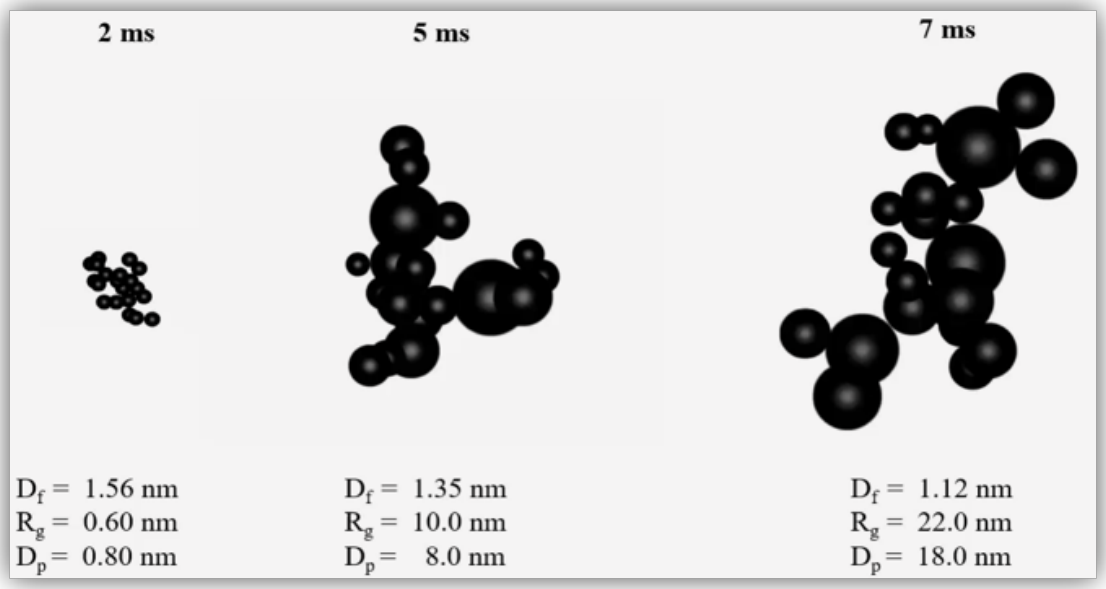

Figure 6.1: Chage of soot morphology with time for 15% EGR O_2 configuration at 36 mm axial locatoin in ECN Spray A combusotion chamber

terms of fractal dimension (D_f) and radius of gyration (R_f). A more robust study is recommended to get the over-all soot formation behavior in internal combustion engines. However, these kind of study is computationally very expensive. Therefore, more research is required to make this kind of soot study computationally affordable.

BIBLIOGRAPHY

[1] R. D. Reitz. Modeling atomization processes in high-pressure vaporizing sprays. *Atomisation Spray Technology*, 3:309–337, 1987.

[2] Nancy J. Brown, Kenneth L. Revzan, and Michael Frenklach. Detailed kinetic modeling of soot formation in ethylene/air mixtures reacting in a perfectly stirred reactor. *Symposium (International) on Combustion*, 27(1):1573–1580, January 1998.

[3] Jörg Appel, Henning Bockhorn, and Michael Frenklach. Kinetic modeling of soot formation with detailed chemistry and physics: laminar premixed flames of c2 hydrocarbons. *Combustion and Flame*, 121(1-2):122–136, April 2000.

[4] Michael Frenklach. Reaction mechanism of soot formation in flames. *Physical Chemistry Chemical Physics*, 4(11):2028–2037, February 2002.

[5] Rolf D Reitz. Spray technology short course. `https://www.erc.wisc.edu/spraycourses.php`, 1996. Accessed: 07-09-2019.

[6] Dhananjay Kumar Srivastava, Avinash Kumar Agarwal, and Tarun Gupta. Effect of engine load on size and number distribution of particulate matter emitted from a direct injection compression ignition engine. *Aerosol and Air Quality Research*, 11(7):915–920, 2011.

[7] H Richter and J.B Howard. Formation of polycyclic aromatic hydrocarbons and their growth to soot—a review of chemical reaction pathways. *Progress in Energy and Combustion Science*, 26(4-6):565–608, August 2000.

[8] Ambient configuration, Engine Combustion Network (ECN). `https://ecn.sandia.gov/diesel-spray-combustion/sandia-cv/ambient-conditions/`. Accessed: 07-09-2019.

[9] E. Cenker, K. Kondo, G. Bruneaux, T. Dreier, T. Aizawa, and C. Schulz. Assessment of soot particle-size imaging with LII at diesel engine conditions. *Applied Physics B*, 119(4):765–776, April 2015.

[10] Gary Borman and Kazuie Nishiwaki. Internal-combustion engine heat transfer. *Progress in Energy and Combustion Science*, 13(1):1–46, January 1987.

[11] P. Furmanski, J. Banaszek, and T. S. Wisniewski. Radiative heat transfer in the combustion chamber of a diesel engine. *International Journal of*

Computational Fluid Dynamics, 11(3-4):325–339, January 1999.

[12] Mark P. B. Musculus. Measurements of the influence of soot radiation on in-cylinder temperatures and exhaust NOx in a heavy-duty DI diesel engine. In *SAE Technical Paper Series*. SAE International, April 2005.

[13] John Abraham and Vinicio Magi. Modeling radiant heat loss characteristics in a diesel engine. In *SAE Technical Paper Series*. SAE International, February 1997.

[14] James F. Wiedenhoefer and Rolf D. Reitz. Multidimensional modeling of the effects of radiation and soot deposition in heavy-duty diesel engines. In *SAE Technical Paper Series*. SAE International, March 2003.

[15] Venkatesh Gopalakrishnan and John Abraham. Computed NO and soot distribution in turbulent transient jets under diesel conditions. *Combustion Science and Technology*, 176(4):603–641, April 2004.

[16] Ramin Houshiar and Cyrus Aghah Najafi. Combustion modelling of soot and radiation with dynamic mesh in CI engines. In *SAE Technical Paper Series*. SAE International, April 2006.

[17] Jian Cai, Shenghui Lei, Adhiraj Dasgupta, Michael F Modest, and Daniel C Haworth. High fidelity radiative heat transfer models for high-pressure laminar hydrogen–air diffusion flames. *Combustion Theory and Modelling*, 18(6):607–626, 2014.

[18] N. Ladommatos, S. M. Abdelhalim, Hua Zhao, and Z. Hu. The dilution, chemical, and thermal effects of exhaust gas recirculation on diesel engine emissions - part 2: Effects of carbon dioxide. In *SAE Technical Paper Series*. SAE International, May 1996.

[19] N. Ladommatos, S. M. Abdelhalim, Hua Zhao, and Z. Hu. Effects of EGR on heat release in diesel combustion. In *SAE Technical Paper Series*. SAE International, February 1998.

[20] Rolf Egnell. The influence of EGR on heat release rate and NO formation in a DI diesel engine. In *SAE Technical Paper Series*. SAE International, June 2000.

[21] John Abraham and Vinicio Magi. Application of the discrete ordinates method to compute radiant heat loss in a diesel engine. *Numerical Heat Transfer, Part A: Applications*, 31(6):597–610, May 1997.

[22] Engine Combustion Network (ECN). https://ecn.sandia.gov. Accessed: 07-09-2019.

[23] Sibendu Som, Gianluca D'Errico, Douglas Longman, and Tommaso Lucchini. Comparison and standardization of numerical approaches for the prediction of non-reacting and reacting diesel sprays. In *SAE Technical Paper Series*. SAE International, April 2012.

[24] Sebastian Ferreyro Fernandez, C. Paul, A. Sircar, A. Imren, D.C. Haworth, S. Roy, and M.F. Modest. Soot and spectral radiation modeling for high-pressure turbulent spray flames. *Combustion and Flame*, 190:402–415, April 2018.

[25] D C Haworth, C Paul, A Sircar, A Imren, S P Roy, W Ge, and M F Modest. Soot and spectral radiation modeling in ECN Spray A and in engines. In *International Multidimensional Engine Modeling User's Group Meeting at the SAE Congress*, Detroit, MI, 2017.

[26] Chandan Paul, Sebastian Ferreyro Fernandez, Daniel C. Haworth, Somesh Roy, and Michael F. Modest. A detailed modeling study of radiative heat transfer in a heavy-duty diesel engine. *Combustion and Flame*, 200:325–341, February 2019.

[27] Muhammad Aqib Chishty, Michele Bolla, Evatt Hawkes, Yuanjiang Pei, and Sanghoon Kook. Assessing the importance of radiative heat transfer for ECN spray a using the transported PDF method. *SAE International Journal of Fuels and Lubricants*, 9(1):100–107, April 2016.

[28] Muhammad A. Chishty, Michele Bolla, Evatt R. Hawkes, Yuanjiang Pei, and Sanghoon Kook. Soot formation modelling for n-dodecane sprays using the transported PDF model. *Combustion and Flame*, 192:101–119, June 2018.

[29] Zongyu Yue and Rolf D. Reitz. Numerical investigation of radiative heat transfer in internal combustion engines. *Applied Energy*, 235:147–163, February 2019.

[30] Somesh P. Roy, Jian Cai, and Michael F. Modest. Development of a multiphase photon Monte Carlo method for spray combustion and its application in high-pressure conditions. *International Journal of Heat and Mass Transfer*, 115:453–466, December 2017.

[31] Hiroaki Watanabe, Ryoichi Kurose, Satoru Komori, and Heinz Pitsch. Effects of radiation on spray flame characteristics and soot formation. *Combustion and Flame*, 152(1-2):2–13, January 2008.

[32] K. Mukut and S. Roy. Effect of EGR and multiphase radiation on pollutant formation in ECN spray-A. *Combustion Theory and Modelling*, Submitted for review.

[33] A. Günther and K.-E. Wirth. Evaporation phenomena in superheated atomization and its impact on the generated spray. *International Journal of Heat and Mass Transfer*, 64:952–965, September 2013.

[34] N. Dombrowski and W.R. Johns. The aerodynamic instability and disintegration of viscous liquid sheets. *Chemical Engineering Science*, 18(3):203–214, March 1963.

[35] Yikai Li and Akira Umemura. Two-dimensional numerical investigation on the dynamics of ligament formation by faraday instability. *International Journal of Multiphase Flow*, 60:64–75, April 2014.

[36] P. G. Drazin and W. H. Reid. *Hydrodynamic Stability*. Cambridge University Press, 2004.

[37] Sergei Sazhin. *Droplets and Sprays*. Springer London, 2014.

[38] G. M. Pai and Shankar Subramaniam. Accurate numerical solution of the spray equation using particle methods. *Atomization and Sprays*, 16(2):159–194, 2006.

[39] C. Baumgarten, H. Lettmann, and G. P. Merker. Modelling of primary and secondary break-up processes in high pressure diesel sprays. CIMAC Congress, 2004.

[40] Rolf D. Reitz and R. Diwakar. Structure of high-pressure fuel sprays. In *SAE Technical Paper Series*. SAE International, February 1987.

[41] Peter J. O'Rourke and Anthony A. Amsden. The tab method for numerical calculation of spray droplet breakup. In *SAE Technical Paper Series*. SAE International, November 1987.

[42] R Schmehl, G Maier, and S Wittig. Cfd analysis of fuel atomization , secondary droplet breakup and spray dispersion in the premix duct of a LPP combustor. In *Eighth International Conference on Liquid Atomization and Spray Systems*, July 2000.

[43] Daero Joung and Kang Y. Huh. 3d RANS simulation of turbulent flow and combustion in a 5 MW reverse-flow type gas turbine combustor. *Journal of Engineering for Gas Turbines and Power*, 132(11):111504, 2010.

[44] L.Y.M. Gicquel, G. Staffelbach, and T. Poinsot. Large eddy simulations of gaseous flames in gas turbine combustion chambers. *Progress in Energy and Combustion Science*, 38(6):782–817, December 2012.

[45] G. Bulat, W.P. Jones, and A.J. Marquis. Large eddy simulation of an industrial gas-turbine combustion chamber using the sub-grid PDF method. *Proceedings of the Combustion Institute*, 34(2):3155–3164, January 2013.

[46] Jorge Amaya, Elena Aguilera Collado, Bénédicte Cuenot, and Thierry Poinsot. Coupling les, radiation and structure in gas turbine simulations. In *Proceedings of the Summer Program*. Center for Turbulence Research, 2010.

[47] W.P. Jones and M.C. Paul. Combination of DOM with LES in a gas turbine combustor. *International Journal of Engineering Science*, 43(5-6):379–397, March 2005.

[48] Jianda Yao and Weicheng Fan. Theory and numerical study on three dimensional discrete transfer radiation model. *Journal of Thermal Science*, 3(4):263–266, December 1994.

[49] S. Chandrasekhar. *Radiative Heat Transfer*. Dover Publications, 1960.

[50] Wenjun Ge, Michael F. Modest, and Somesh P. Roy. Development of high-order P models for radiative heat transfer in special geometries and boundary conditions. *Journal of Quantitative Spectroscopy and Radiative Transfer*, 172:98–109, March 2016.

[51] Michael F. Modest and Jun Yang. Elliptic PDE formulation and boundary conditions of the spherical harmonics method of arbitrary order for general three-dimensional geometries. *Journal of Quantitative Spectroscopy and Radiative Transfer*, 109(9):1641–1666, June 2008.

[52] Sangtae Jeon and Yongmo Kim. Multi-environment probability density function modeling for turbulent CH_4 flames under moderate or intense low-oxygen dilution combustion conditions with recirculated flue gases. *Energy & Fuels*, 31(8):8685–8697, July 2017.

[53] Michael F Modest. Radiative exchange between nonideal surfaces. In *Radiative Heat Transfer*. Elsevier, 2013.

[54] L.S. Rothman, I.E. Gordon, R.J. Barber, H. Dothe, R.R. Gamache, A. Goldman, V.I. Perevalov, S.A. Tashkun, and J. Tennyson. HITEMP, the high-temperature molecular spectroscopic database. *Journal of Quantitative Spectroscopy and Radiative Transfer*, 111(15):2139–2150, October 2010.

[55] M.Y. Choi, A. Hamins, G.W. Mulholland, and T. Kashiwagi. Simultaneous optical measurement of soot volume fraction and temperature in premixed flames. *Combustion and Flame*, 99(1):174–186, October 1994.

[56] Dale R. Tree and Kenth I. Svensson. Soot processes in compression ignition engines. *Progress in Energy and Combustion Science*, 33(3):272–309, June 2007.

[57] Ian M Kennedy. Models of soot formation and oxidation. *Progress in Energy and Combustion Science*, 23(2):95–132, January 1997.

[58] Scott A. Skeen, Julien Manin, Lyle M. Pickett, Emre Cenker, Gilles Bruneaux, Katsufumi Kondo, Tets Aizawa, Fredrik Westlye, Kristine Dalen, Anders Ivarsson, Tiemin Xuan, Jose M Garcia-Oliver, Yuanjiang Pei, Sibendu Som, Wang Hu, Rolf D. Reitz, Tommaso Lucchini, Gianluca D'Errico, Daniele Farrace, Sushant S. Pandurangi, Yuri M. Wright, Muhammad Aqib Chishty, Michele Bolla, and Evatt Hawkes. A progress review on soot experiments and modeling in the engine combustion network (ECN). *SAE International Journal of Engines*, 9(2):883–898, April 2016.

[59] R. J. GILL and D. B. OLSON. Estimation of soot thresholds for fuel mixtures. *Combustion Science and Technology*, 40(5-6):307–315, September 1984.

[60] Liming Li and Peter B. Sunderland. Smoke points of fuel–fuel and fuel–inert mixtures. *Fire Safety Journal*, 61:226–231, October 2013.

[61] D.M Probert I. M Khan, G. Greeves. Prediction of soot and nitric oxide concentrations in diesel engine exhaust. *Air Pollution Control in Transport Engines, Institute of Mechanical Engineers, London*, Paper C142:205–217, 1971.

[62] Ian M. Kennedy, Wolfgang Kollmann, and J.-Y. Chen. A model for soot formation in a laminar diffusion flame. *Combustion and Flame*, 81(1):73–85, July 1990.

[63] K.M. Leung, R.P. Lindstedt, and W.P. Jones. A simplified reaction mechanism for soot formation in nonpremixed flames. *Combustion and Flame*, 87(3-4):289–305, December 1991.

[64] P.A. Tesner, E.I. Tsygankova, L.P. Guilazetdinov, V.P. Zuyev, and G.V. Loshakova. The formation of soot from aromatic hydrocarbons in diffusion flames of hydrocarbon-hydrogen mixtures. *Combustion and Flame*, 17(3):279–285, December 1971.

[65] M. von Smoluchowski. Versuch einer mathematischen theorie der koagulationskinetik kolloider. *Lösungen Physics*, 17:557, 1916.

[66] Michael Balthasar and Michael Frenklach. Monte-carlo simulation of soot particle coagulation and aggregation: the effect of a realistic size distribution. *Proceedings of the Combustion Institute*, 30(1):1467–1475, January 2005.

[67] Andrei Kazakov and Michael Frenklach. Dynamic modeling of soot particle coagulation and aggregation: Implementation with the method of moments and application to high-pressure laminar premixed flames. *Combustion and Flame*, 114(3-4):484–501, August 1998.

[68] Michael Frenklach and Hai Wang. Detailed modeling of soot particle nucleation and growth. *Symposium (International) on Combustion*, 23(1):1559–1566, January 1991.

[69] M. B. Colket and R. J. Hall. Description and discussion of a detailed model for soot formation in laminar premixed flames. pages UTRC91–20, 1991.

[70] R.P. Lindstedt and S.A. Louloudi. Joint-scalar transported PDF modeling of soot formation and oxidation. volume 30, pages 775–783. Elsevier BV, January 2005.

[71] Fred Gelbard, Yoram Tambour, and John H Seinfeld. Sectional representations for simulating aerosol dynamics. *Journal of Colloid and Interface Science*, 76(2):541–556, August 1980.

[72] Michael Frenklach. Method of moments with interpolative closure. *Chemical Engineering Science*, 57(12):2229–2239, 2002.

[73] Michael Frenklach and Stephen J. Harris. Aerosol dynamics modeling using the method of moments. *Journal of Colloid and Interface Science*, 118(1):252–261, July 1987.

[74] Robert McGraw. Description of aerosol dynamics by the quadrature method of moments. *Aerosol Science and Technology*, 27(2):255–265, January 1997.

[75] Matthew Celnik, Robert Patterson, Markus Kraft, and Wolfgang Wagner. Coupling a stochastic soot population balance to gas-phase chemistry using operator splitting. *Combustion and Flame*, 148(3):158–176, February 2007.

[76] Robert I.A. Patterson, Jasdeep Singh, Michael Balthasar, Markus Kraft, and Wolfgang Wagner. Extending stochastic soot simulation to higher pressures. *Combustion and Flame*, 145(3):638–642, May 2006.

[77] Matthew Celnik, Abhijeet Raj, Richard West, Robert Patterson, and Markus Kraft. Aromatic site description of soot particles. *Combustion and Flame*, 155(1-2):161–180, October 2008.

[78] Matthew S. Celnik, Markus Sander, Abhijeet Raj, Richard H. West, and Markus Kraft. Modelling soot formation in a premixed flame using an aromatic-site soot model and an improved oxidation rate. *Proceedings of the Combustion Institute*, 32(1):639–646, 2009.

[79] Abhijeet Raj, Matthew Celnik, Raphael Shirley, Markus Sander, Robert Patterson, Richard West, and Markus Kraft. A statistical approach to develop a detailed soot growth model using PAH characteristics. *Combustion and Flame*, 156(4):896–913, April 2009.

[80] Lyle M. Pickett, Caroline L. Genzale, Gilles Bruneaux, Louis-Marie Malbec, Laurent Hermant, Caspar Christiansen, and Jesper Schramm. Comparison of diesel spray combustion in different high-temperature, high-pressure facilities. *SAE International Journal of Engines*, 3(2):156–181, October 2010.

[81] S.H. EL TAHRY. k-epsilon equation for compressible reciprocating engine flows. *Journal of Energy*, 7(4):345–353, July 1983.

[82] OpenFOAM 2.3.X CFD Toolbox. `http://www.openfoam.org`. Accessed: 07-09-2019.

[83] S. James, M. S. Anand, M. K. Razdan, and S. B. Pope. In situ detailed chemistry calculations in combustor flow analyses. *Journal of Engineering for Gas Turbines and Power*, 123(4):747, 2001.

[84] John K. Dukowicz. A particle-fluid numerical model for liquid sprays. *Journal of Computational Physics*, 35(2):229–253, April 1980.

[85] Tong Yao, Yuanjiang Pei, Bei-Jing Zhong, Sibendu Som, Tianfeng Lu, and Kai Hong Luo. A compact skeletal mechanism for n-dodecane with optimized semi-global low-temperature chemistry for diesel engine simulations. *Fuel*, 191:339–349, March 2017.

[86] Somesh Roy. *Aerosol-dynamics-based soot modeling of flames*. PhD thesis, The Pennsylvania State Universtiy, 2014.

[87] Amit Bhave and Markus Kraft. Partially stirred reactor model: Analytical solutions and numerical convergence study of a PDF/Monte Carlo method. *SIAM Journal on Scientific Computing*, 25(5):1798–1823, January 2004.

[88] Somesh P. Roy and Daniel C. Haworth. A systematic comparison of detailed soot models and gas-phase chemical mechanisms in laminar premixed flames. *Combustion Science and Technology*, 188(7):1021–1053, February 2016.

[89] H Wang, D X Du, C J Sung, and C K Law. Experiments and numerical simulation on soot formation in opposed-jet ethylene diffusion flames. *Proceedings of the Combustion Institute*, 26:2359–2368, 1996.

[90] M Frenklach and H Wang. Detailed mechanism and modeling of soot particle formation. In H Bockhorn, editor, *Soot Formation in Combustion: Mechanisms and Models*. Springer-Verlag, New York, 1994.

[91] Gopalendu Pal, Ankur Gupta, Michael F. Modest, and Daniel C. Haworth. Comparison of accuracy and computational expense of radiation models in simulation of non-premixed turbulent jet flames. *Combustion and Flame*, 162(6):2487–2495, June 2015.

[92] Anquan Wang and Michael F. Modest. Photon monte carlo simulation for radiative transfer in gaseous media represented by discrete particle fields. *Journal of Heat Transfer*, 128(10):1041, 2006.

[93] H. Chang and T. T. Charalampopoulos. Determination of the wavelength dependence of refractive indices of flame soot. *Proceedings of the Royal Society A: Mathematical, Physical and Engineering Sciences*, 430(1880):577–591, September 1990.

[94] A. Tuntomo, C. L. Tien, and S. H. Park. Optical constants of liquid hydrocarbon fuels. *Combustion Science and Technology*, 84(1):133–140, July 1992.

[95] Leonid A. Dombrovsky. Thermal radiation from nonisothermal spherical particles, 2008.

[96] L Dombrovsky. Spectral properties of diesel fuel droplets. *Fuel*, 82(1):15–22, January 2003.

[97] Pressure based ignition delay, Engine Combustion Network (ECN). `https://ecn.sandia.gov/diesel-spray-combustion/experimental-diagnostics/`. Accessed: 07-09-2019.

[98] O. Samimi Abianeh, M. Levins, and C. P. Chen. Pressure-based ignition delay times of non-premixed turbulent jet flames using various turbulence models. In *ASME 2016 Internal Combustion Engine Fall Technical Conference*. ASME, October 2016.

[99] Michele Bolla, Daniele Farrace, Yuri M. Wright, Konstantinos Boulouchos, and Epaminondas Mastorakos. Influence of turbulence–chemistry interaction forn-heptane spray combustion under diesel engine conditions with emphasis on soot formation and oxidation. *Combustion Theory and Modelling*, 18(2):330–360, March 2014.

[100] Yuanjiang Pei, Evatt R. Hawkes, and Sanghoon Kook. A comprehensive study of effects of mixing and chemical kinetic models on predictions of n-heptane jet ignitions with the PDF method. *Flow, Turbulence and Combustion*, 91(2):249–280, April 2013.

[101] Subhasish Bhattacharjee and Daniel C. Haworth. Simulations of transient n-heptane and n-dodecane spray flames under engine-relevant conditions using a transported PDF method. *Combustion and Flame*, 160(10):2083–2102, October 2013.

[102] Khaled Mosharraf Mukut and Somesh P Roy. A sensitivity study on soot and no_x formation in high pressure combustion system. In *2018 Spring Technical Meeting of Central States Section of the Combustion Institute*, Minneapolis, MN., 2018.

[103] Zhuohui J. He, Clarence Chang, and Caitlin Follen. NO_X emissions performance and correlation equations for a multipoint LDI injector. In *53rd AIAA Aerospace Sciences Meeting*. American Institute of Aeronautics and Astronautics, January 2015.

[104] Nancy J. Brown, Lucas A.J. Bastien, and Phillip N. Price. Transport properties for combustion modeling. *Progress in Energy and Combustion Science*, 37(5):565–582, September 2011.